Monthly Notices
of the
ROYAL ASTRONOMICAL SOCIETY

MNRAS **445,** 1774–1796 (2014) doi:10.1093/mnras/stu1788

Cosmological simulations of galaxy clusters with feedback from active galactic nuclei: profiles and scaling relations

Simon R. Pike,[1⋆] Scott T. Kay,[1] Richard D. A. Newton,[1,2] Peter A. Thomas[3] and Adrian Jenkins[4]

[1]*Jodrell Bank Centre for Astrophysics, School of Physics and Astronomy, The University of Manchester, Manchester M13 9PL, UK*
[2]*International Centre for Radio Astronomy Research, University of Western Australia, 35 Stirling Highway, Crawley, WA 6009, Australia*
[3]*Astronomy Centre, University of Sussex, Falmer, Brighton BN1 9QH, UK*
[4]*Institute for Computational Cosmology, Department of Physics, University of Durham, Durham DH1 3LE, UK*

Accepted 2014 August 28. Received 2014 August 27; in original form 2014 April 25

ABSTRACT

We present results from a new set of 30 cosmological simulations of galaxy clusters, including the effects of radiative cooling, star formation, supernova feedback, black hole growth and AGN feedback. We first demonstrate that our AGN model is capable of reproducing the observed cluster pressure profile at redshift, $z \simeq 0$, once the AGN heating temperature of the targeted particles is made to scale with the final virial temperature of the halo. This allows the ejected gas to reach larger radii in higher mass clusters than would be possible had a fixed heating temperature been used. Such a model also successfully reduces the star formation rate in brightest cluster galaxies and broadly reproduces a number of other observational properties at low redshift, including baryon, gas and star fractions, entropy profiles outside the core and the X-ray luminosity–mass relation. Our results are consistent with the notion that the excess entropy is generated via selective removal of the densest material through radiative cooling; supernova and AGN feedback largely serve as regulation mechanisms, moving heated gas out of galaxies and away from cluster cores. However, our simulations fail to address a number of serious issues; for example, they are incapable of reproducing the shape and diversity of the observed entropy profiles within the core region. We also show that the stellar and black hole masses are sensitive to numerical resolution, particularly the gravitational softening length; a smaller value leads to more efficient black hole growth at early times and a smaller central galaxy.

Key words: hydrodynamics – methods: numerical – galaxies: clusters: general – X-rays: galaxies: clusters.

1 INTRODUCTION

It has long been known that the observable properties of the intracluster medium (ICM hereafter), especially X-ray luminosity, do not scale with mass as expected if gravitational heating is the only important physical process at work (e.g. Voit, Kay & Bryan 2005). Ponman, Cannon & Navarro (1999) confirmed that the reason for this *similarity breaking* is due to low-mass groups and clusters having excess entropy in their cores. A large body of work has since been accumulating using X-ray data, measuring the detailed thermal structure of the ICM and how it depends on cluster mass, redshift and dynamical state (e.g. Vikhlinin et al. 2006; Pratt et al. 2009; Sun 2012; Eckert et al. 2013).

Complementary to the X-ray work, observations of the Sunyaev–Zel'dovich (hereafter SZ) effect (Sunyaev & Zeldovich 1972) are now providing independent measurements of the ICM pressure distribution and scaling relations (e.g. Andersson et al. 2011; Planck Collaboration 2011, 2013; Marrone et al. 2012; Sifón et al. 2013). Furthermore, optical–infrared studies are measuring the stellar mass component, both in galaxies and the intracluster light (ICL; e.g. Stott et al. 2011; Lidman et al. 2012; Budzynski et al. 2014). It is clear that the majority of the baryons are in the ICM, with only a few per cent of the total cluster mass locked in stars.

The physical origin of the excess entropy (and why star formation is so inefficient) continues to be a subject of debate. Early work suggested that the ICM was pre-heated at high redshift, prior to cluster formation (Evrard & Henry 1991; Kaiser 1991). However, cluster models with pre-heating have shown that it produces isentropic cores in low-mass systems (e.g. Borgani et al. 2001; Babul et al. 2002), at odds with the observational data (e.g. Ponman, Sanderson

⋆E-mail: simon.pike-2@postgrad.manchester.ac.uk

& Finoguenov 2003). Pre-heating simulations that include radiative cooling also tend to produce too little star formation, but this somewhat depends on numerical resolution (e.g. Muanwong et al. 2002).

An alternative model is to exploit the radiative cooling of gas directly. As the lowest entropy gas cools and forms stars, it allows the remaining, higher entropy material to flow towards the centre of the cluster, creating an overall excess in the core. Since this effect is more prominent in lower mass systems where the cooling time is shorter, it leads to the desired outcome (Bryan 2000). The *radiative* model was confirmed with fully cosmological simulations (e.g. Pearce et al. 2000; Muanwong et al. 2001; Davé, Katz & Weinberg 2002) but it is ultimately flawed as it requires an unrealistic amount of gas to cool and form stars (the so-called *overcooling* problem; see Balogh et al. 2001; Borgani et al. 2002).

The most promising solution to both entropy and overcooling problems is negative *feedback*, i.e. energetic galactic outflows that remove the densest gas and reduce the star formation efficiency in galaxies. The first models focused on supernova feedback but these fail to produce enough entropy to remove material from cluster cores (e.g. Borgani et al. 2004) unless the energy is targeted at a small amount of mass (e.g. Kay, Thomas & Theuns 2003; Kay 2004). A more appealing solution, on energetic grounds, is feedback from active galactic nuclei (AGN; e.g. Wu, Fabian & Nulsen 2000), where around 10 per cent of the mass accreted on to a supermassive black hole (BH) is potentially available as feedback energy. High-resolution X-ray observations have now firmly established that AGN are interacting with the ICM in low-redshift clusters through the production of jet-induced cavities and weak shocks (e.g. Fabian 2012; McNamara & Nulsen 2012). It is also likely that BHs are even more active in high-redshift clusters, given that the space density of quasars peaks at $z \simeq 2$ (Shaver et al. 1996).

Including AGN feedback in cosmological simulations is a highly non-trivial task, given the disparity in scales between the accreting BH (<1 pc) and the host galaxy (∼10 kpc). As a result, a range of models for both the accretion and feedback processes have been developed and applied to simulations of galaxies (e.g. Springel, Di Matteo & Hernquist 2005a; Booth & Schaye 2009; Power, Nayakshin & King 2011; Newton & Kay 2013). Due to the infancy of these models, much of the simulation work on cluster scales has been done using idealized, or cosmologically influenced, initial conditions (e.g. Morsony et al. 2010; Gaspari et al. 2011; Hardcastle & Krause 2013). However, a growing number of groups are now starting to incorporate AGN feedback in fully cosmological simulations of groups and clusters, with some success. We summarize a few of their results below.

Sijacki et al. (2007) included models for both a *quasar* mode (heating the gas local to the BH) and a *radio* mode (injecting bubbles into the ICM when the accretion rate is low), showing that such feedback could produce a realistic entropy profile in clusters while suppressing their cooling flows. Puchwein, Sijacki & Springel (2008) and Puchwein et al. (2010) applied this model to a larger cosmological sample of clusters and showed that the AGN feedback reduced the overcooling on to brightest cluster galaxies (BCGs), resulting in X-ray and optical properties that are more realistic, but producing a large fraction of intracluster stars. Dubois et al. (2011) ran a cosmological re-simulation of a cluster and were also able to prevent overcooling with AGN feedback, producing gas profiles that were consistent with cool-core clusters when metallicity effects were neglected. Fabjan et al. (2010) ran re-simulations for 16 clusters and found that BCG growth was sufficiently quenched at redshifts, $z < 4$, and their runs produced reasonable temperature profiles of galaxy groups. However in massive clusters, the AGN model is unable to create cool cores, producing an excess of entropy within r_{2500}. Planelles et al. (2013) further showed that AGN feedback in their simulations is capable of reproducing observed cluster baryon, gas and star fractions. Short et al. (2010) included AGN feedback into cosmological simulations using a semi-analytic galaxy formation model to infer the heating rates from the full galaxy population and showed that such a model could reproduce a range of X-ray cluster properties, although they neglected the effects of radiative cooling (however, see also Short, Thomas & Young 2013). McCarthy et al. (2010, 2011) simulated the effects of AGN feedback in galaxy groups and showed that they could reproduce a number of their observed properties. Their feedback model, based on Booth & Schaye (2009), works by ejecting high-entropy gas out of the cores of proto-group haloes at high redshift and thus generates the excess entropy in a similar way to the *radiative* model described above, while also regulating the amount of star formation.[1]

In this paper, we introduce a new set of cosmological simulations of clusters and use them to further our understanding of how non-gravitational processes (especially AGN feedback) affect such systems, comparing to observational data where appropriate. Our study has the following particular strengths. First, we have selected a representative sample of clusters to assess their properties across the full cluster mass range. Secondly, all objects have around the same number of particles within their virial radius at $z = 0$, removing potential bias due to low-mass systems being less well resolved. Thirdly, we have run our simulations several times, incrementally adding radiative cooling and star formation, supernova feedback and AGN feedback. This allows us to assess the relative effects of these individual components. Finally, we use the AGN feedback model from Booth & Schaye (2009); since we apply it to cluster scales, our results complement those on group scales by McCarthy et al. (2010). In particular, we show that our simulations can reproduce observed ICM pressure profiles at $z \simeq 0$ particularly well, once the AGN heating temperature is adjusted to scale with the final virial temperature of the cluster.

The remainder of the paper is laid out as follows. Section 2 provides details of the sample selection, our implementation of the sub-grid physics and the method by which radial profiles and scaling relations are estimated. Our main results are then presented in Sections 3 (global baryonic properties), 4 (radial profiles) and 5 (scaling relations). In Section 6, we present a resolution study before drawing conclusions and discussing our results in the context of recent work by others (Le Brun et al. 2014; Planelles et al. 2013, 2014) in Section 7.

2 SIMULATION DETAILS

Our main results are based on a sample of 30 clusters, re-simulated from a large cosmological simulation of structure formation within the Λ cold dark matter cosmology. The sample size was chosen as it was deemed to be large enough to produce reasonable statistical estimates of cluster properties over the appropriate range of masses and dynamical states, while small enough to allow a competitive resolution to be used. We outline how the clusters were selected below, before summarizing details of the baryonic physics in our simulations.

[1]This mechanism was originally described in a model by Voit & Bryan (2001), who phrased it in terms of feedback from supernovae.

2.1 Cluster sample

The clusters were selected from the Virgo Consortium's MR7 dark matter-only simulation, available online via the Millennium data base.[2] The simulation also features in Guo et al. (2013) with the name MS-W7. It is similar to the original Millennium simulation (Springel et al. 2005b), with 2160^3 particles within a $500\,h^{-1}$ Mpc comoving volume, but uses different cosmological parameters and phases. The cosmological parameters are consistent with the *Wilkinson Microwave Anisotropy Probe* 7 year data (Komatsu et al. 2011), with $\Omega_{\rm m} = 0.272$, $\Omega_\Lambda = 0.728$, $\Omega_{\rm b} = 0.0455$, $h = 0.704$ and $\sigma_8 = 0.81$. The phases for the MR7 volume were taken from the public multiscale Gaussian white noise field Panphasia (Jenkins 2013; referred to as MW7 in their table 6).

Clusters were identified in the parent simulation at $z = 0$ using the Friends-of-Friends algorithm (Davis et al. 1985) with dimensionless linking length, $b = 0.2$. The SUBFIND (Springel et al. 2001) routine was also run on the fly and we used the position of the particle with the minimum energy (from the most massive sub-halo within each Friends-of-Friends group) to define the cluster centre. We subdivided the clusters with masses $10^{14} < \log_{10}(M_{200}/h^{-1}\,{\rm M}_\odot) < 10^{15}$ into five mass bins, equally spaced in $\log_{10}(M_{200})$.[3] Six objects were then chosen at random from within each bin, yielding a sample of 30 objects. Particle IDs within $3r_{200}$ (centred on the most bound particle) were recorded and their coordinates at the initial redshift ($z = 128$) used to define a Lagrangian region to be re-simulated at higher resolution. Finally, initial conditions were generated for each object with a particle mass chosen to produce a fixed number of particles within r_{200}, $N_{200} \simeq 10^6$. The advantage of this choice is that the same dynamic range in internal substructure is resolved within each object, regardless of its mass. The particle mass varies from $m = 1 \times 10^8\,h^{-1}\,{\rm M}_\odot$ for the lowest mass clusters to $m = 8 \times 10^8\,h^{-1}\,{\rm M}_\odot$ for the highest mass clusters.

The method used to make the initial conditions for the re-simulations was essentially that described in Springel et al. (2008) for the Aquarius project. The large-scale power, from Panphasia, was reproduced and uncorrelated small-scale power added to the high-resolution region down to the particle Nyquist frequency of that region. These initial conditions were created before the re-simulation method described in Jenkins (2013) was developed. This means that the added small-scale power was an independent realization and distinct from that given by the Panphasia field itself.

Each cluster was run several times using a modified version of the GADGET-2 *N*-body/smoothed particle hydrodynamics (SPH) code (Springel 2005), first with dark matter (DM) only, then with gas and varying assumptions for the baryonic physics (discussed below). The gas initial conditions were identical to the DM-only case, except that we split each particle within the Lagrangian region into a gas particle with mass, $m_{\rm gas} = (\Omega_{\rm b}/\Omega_{\rm m})m$, and a DM particle with mass, $m_{\rm DM} = m - m_{\rm gas}$. The gravitational softening length was fixed in physical coordinates for $z < 3$, setting the equivalent Plummer value to $\epsilon = 4r_{200}/\sqrt{N_{200}}$ following Power et al. (2003). Thus, in our lowest mass clusters $\epsilon \simeq 3\,h^{-1}$ kpc, increasing by a factor of 2 for our highest mass clusters. The softening was fixed in comoving coordinates at $z > 3$. For the gas, the SPH smoothing length was never allowed to become smaller than the softening length, given that gravitational forces become inaccurate below this value.

[2] http://gavo.mpa-garching.mpg.de/Millennium/

[3] The mass, M_{200}, is that contained within a sphere of radius r_{200}, enclosing a mean density of 200 times the critical density of the Universe.

Table 1. Summary of the models used for our cluster simulations with baryonic physics.

Model	Cooling and SF	Supernovae	AGN
NR	No	No	No
CSF	Yes	No	No
SFB	Yes	Yes	No
AGN	Yes	Yes	Yes

2.2 Baryonic physics

For our main results, we performed four sets of runs with gas and additional, non-gravitational physics. The first model (labelled NR) used non-radiative gas dynamics only. For the second set of runs, we included radiative cooling and star formation (CSF); in the third, we added supernova feedback (SFB); and in the fourth we additionally modelled feedback from active galactic nuclei (AGN). Table 1 summarizes these choices. We discuss the details of each process below and refer to Newton & Kay (2013) for further information.

2.2.1 *Radiative cooling and star formation*

Gas particles with temperatures $T > 10^4$ K are allowed to cool radiatively. We assume collisional ionization equilibrium and the gas is isochoric when calculating the energy radiated across each time-step, following Thomas & Couchman (1992). Cooling rates are calculated using the tables given by Sutherland & Dopita (1993) for a zero-metallicity gas. (We note the lack of metal enrichment is a limitation of the simulations and its effect on the cooling rate will likely be important at high redshift in particular.)

For redshifts $z < 10$ and densities $n_{\rm H} < 0.1\,{\rm cm}^{-3}$, a temperature floor of 10^4 K is imposed, approximating the effect of heating from a UV background (although this has no effect on our cluster simulations). Above this density and at all redshifts, the gas is assumed to be a multiphase mixture of cold molecular clouds, warm atomic gas and hot ionized bubbles, all approximately in pressure equilibrium. Following Schaye & Dalla Vecchia (2008), we model this using a polytropic equation of state

$$P = A\,n_{\rm H}^{\gamma_{\rm eff}}, \tag{1}$$

where P is the gas pressure, A is a constant (set to ensure that $T = 10^4$ K at $n_{\rm H} = 0.1\,{\rm cm}^{-3}$) and $\gamma_{\rm eff} = 4/3$, causing the Jeans mass to be independent of density (Schaye & Dalla Vecchia 2008). Gas is allowed to leave the equation of state if its thermal energy increases by at least 0.5 dex, or if it is heated by a nearby supernova or AGN.

Each gas particle found on the equation of state is given a probability to form a star particle following the method of Schaye & Dalla Vecchia (2008). This is designed to match the observed Kennicutt–Schmidt law for a disc whose thickness is approximately equal to the Jeans length (i.e. the gas is hydrostatically supported perpendicular to the disc plane). We assume a disc gas mass fraction, $f_{\rm g} = 1$,[4] and a Salpeter IMF when calculating the star formation rate, which can be expressed as

$$\dot{m}_* = 5.99 \times 10^{-10}\,{\rm M}_\odot\,{\rm yr}^{-1} \left(\frac{m_{\rm gas}}{1\,{\rm M}_\odot}\right) \left(\frac{P/k}{10^3\,{\rm cm}^{-3}\,{\rm K}}\right)^{0.2}. \tag{2}$$

[4] While this is not true in practice, the star formation rate depends weakly on the gas fraction, $\dot{\rho}_* \propto f_{\rm g}^{0.2}$, as discussed in Schaye & Dalla Vecchia (2008).

It thus follows that the estimated probability of a given gas particle forming a star, $p_\star$, is given by

$$p_* = \min\left(\frac{\dot{m}_* \, \Delta t}{m_{\rm gas}}, 1\right), \tag{3}$$

where Δt is the current time-step of the particle.

2.2.2 *Supernova feedback*

Supernova feedback is an important mechanism for re-heating interstellar gas following star formation. In addition to this effect (which is already accounted for in our equation of state, above), we also assume that supernovae produce galactic winds. The method used here follows the prescription outlined in Dalla Vecchia & Schaye (2012). The dominant contribution comes from the Type II (core-collapse) supernovae, which occur shortly after formation (up to ~ 10 Myr); for simplicity we neglect this short delay. The temperature to which a supernova event (associated with a newly formed star particle) can heat the surrounding gas particles, $T_{\rm SN}$, is calculated as

$$T_{\rm SN} = 2.65 \times 10^7 \ {\rm K} \left(\frac{\epsilon_{\rm SN}}{N_{\rm SN}} \frac{m_{\rm star}}{m_{\rm gas}}\right), \tag{4}$$

where $\epsilon_{\rm SN}$ is the fraction of supernova energy available for heating, $N_{\rm SN}$ is the number of particles to be heated and $m_{\rm star}$ is the star particle mass (we set $m_{\rm star} = m_{\rm gas}$). When calculating this temperature we have assumed that the total energy released per supernovae $E_{\rm SN} = 10^{51}$ erg. For our main results (see below), we fix $T_{\rm SN} = 10^7$ K and $N_{\rm SN} = 3$, implying an efficiency $\epsilon_{\rm SN} \simeq 1.1$ for a Salpeter IMF (or $\epsilon_{\rm SN} \simeq 0.7$ for a Chabrier IMF, which predicts relatively more high-mass stars). We discuss variations in the heating parameters below.

2.2.3 *BH growth and AGN feedback*

BHs are usually included as collisionless sink particles within cosmological simulations, with an initial seed placed in every Friends-of-Friends group that is newly resolved by the simulation. This requires the group finder to be run on the fly; our code is currently unable to perform this task, instead we place our seed BHs at a fixed (high) redshift. Specifically, we take the snapshot at redshift $z_{\rm ini}$ from our SFB model and find all sub-haloes with mass $M > M_{\rm sub}$ replacing the most bound (gas or star) particle with a BH particle (leaving the particle mass, position and velocity unchanged). For our default AGN model, we assume $z_{\rm ini} = 5.2$ and set $M_{\rm sub}$ to a value that is approximately equal to the mass of 50 DM particles. Tests revealed the final hot gas and stellar distributions to be insensitive to the choice of these parameters. This is because most of the AGN feedback originates from the central BH, which gets most of its mass from accretion in the cluster at much lower redshift ($z < 2$; see Fig. 15 in Section 6).

BH accretion and AGN feedback rates are modelled via the Booth & Schaye (2009) method, based on the original approach by Springel et al. (2005a). BHs grow both via accretion of the surrounding gas and mergers with other BHs. Since discreteness effects are severe for all but the most massive BHs, a second *internal* mass variable is tracked to ensure that the accretion of the gas on to the central BH can be modelled smoothly. We give each BH an initial internal mass of $10^5 \, h^{-1} \, {\rm M}_\odot$. All local properties are then estimated by adopting the SPH method for each BH particle. A smoothing length is determined adaptively by enclosing a fixed number of neighbours, but it cannot go lower than the gravitational softening scale. In practice, smoothing lengths for central BHs are nearly always set to this minimum value which limits the estimate of the local gas density.

Accretion occurs at a rate set by the minimum of the Bondi–Hoyle–Lyttleton (Hoyle & Lyttleton 1939) and Eddington values

$$\dot{M}_{\rm BH} = \min\left[\alpha \frac{4\pi G^2 M_{\rm BH}^2 \rho_{\rm gas}}{(c_{\rm s}^2 + v^2)^{3/2}}, \frac{4\pi G m_{\rm H} M_{\rm BH}}{\epsilon_{\rm r} \sigma_{\rm T} c}\right], \tag{5}$$

where $M_{\rm BH}$ is the internal black hole mass, $\epsilon_{\rm r}$ the efficiency of mass–energy conversion, $\rho_{\rm gas}$ the local gas density, $c_{\rm s}$ the sound speed and v the relative velocity of the BH with respect to the gas it inhabits. The value of α is calculated following Booth & Schaye (2009), as

$$\alpha = \max\left[\left(\frac{n_{\rm H}}{0.1 \ {\rm cm}^{-3}}\right)^2, 1\right], \tag{6}$$

which attempts to correct for the mismatch in scales between where the gas properties are estimated and where the accretion would actually be going on.[5] If the internal mass exceeds the particle mass (set initially to $m_{\rm gas}$), neighbouring gas particles are removed from the simulation at the appropriate rate. BHs may also grow via mergers with other BHs, when the least massive object comes within the smoothing radius of the more massive object and the two are gravitationally bound.[6] The latter is irrelevant in practice as we force the position of a BH to be at the local potential minimum. This leads to some overmerging of BHs but avoids spurious scattering, causing the accretion (and therefore feedback) rate to be severely underestimated.

For the AGN feedback, the heating rate is assumed to scale with the accretion rate as

$$\dot{E}_{\rm AGN} = \epsilon_{\rm f} \epsilon_{\rm r} \dot{M}_{\rm BH} c^2, \tag{7}$$

where $\epsilon_{\rm f}$ is the efficiency with which the energy couples to the gas. For our default models, we set both efficiency parameters to the values used in Booth & Schaye (2009), namely $\epsilon_{\rm f} = 0.15$ and $\epsilon_{\rm r} = 0.1$.

Due to the limitations in resolution, it is unclear what the best method for distributing the energy is. In order to create outflows, the surrounding gas needs to be given enough energy to rise out of the potential well, before it is able to radiate it away. In order to achieve this, an amount of feedback energy, $E_{\rm crit}$, is stored until there is enough to heat at least $N_{\rm AGN}$ neighbouring gas particles to a temperature $T_{\rm AGN}$, i.e.

$$E_{\rm crit} = N_{\rm AGN} \, m_{\rm gas} \, \frac{3}{2} \frac{k T_{\rm AGN}}{\mu m_{\rm H}}, \tag{8}$$

where $\mu = 0.59$ is the mean atomic weight for an ionized gas with primordial ($X = 0.76$, $Z = 0$) composition. In our default AGN model, we set $N_{\rm AGN} = 1$ (i.e. heat a minimum of one particle at a time) but vary $T_{\rm AGN}$ in proportion to the final virial temperature of the cluster (from $T_{\rm AGN} = 10^8$K in the lowest mass objects to $10^{8.5}$K at the highest mass (further details are given below).

[5]Note that in this method the accretion rate is a strong function of gas density when sub-Eddington $\dot{M}_{\rm BH} \propto \rho_{\rm gas}^3$.

[6]We note that BH particle mass is conserved in our simulations; thus, when many mergers occur at high redshift, the mass of a BH particle can significantly exceed its internal mass.

2.3 Calculation of cluster properties

For our main results, we focus on the radial distribution of observable cluster properties (profiles) and the scaling of integrated properties with mass (cluster scaling relations). Unless specified, we measure all properties within a radius r_{500}, as this is the most common scale used for the observational data. Details of how we calculate these properties are provided in Appendix A; we also summarize the observational data that we compare our results with in Appendix B.

An issue that we report here is the large discrepancy between spectroscopic-like temperature $T_{\rm sl}$ (a proxy for X-ray temperature; Mazzotta et al. 2004) and mass-weighted temperature $T_{\rm m}$ (more relevant for SZ observations). The former was found to be significantly lower (and noisier) than the latter in our simulations. For the AGN model, the ratio between the two temperatures at $z = 0$ varies from $T_{\rm sl}/T_{\rm m} = 0.6$–$0.7$ in low-mass clusters, decreasing to 0.3–0.4 in high-mass clusters. It is particularly problematic for the most massive clusters, where the virial temperature is significantly higher than the cut-off temperature for calculating $T_{\rm sl}$ (0.5 keV).

The origin of this discrepancy is two-fold. First, large, X-ray bright substructures may contain gas that is sufficiently cold and dense to produce a significant bias in the spectroscopic-like temperature. Such a substructure would normally be masked out of X-ray images (e.g. Nagai, Vikhlinin & Kravtsov 2007a). Secondly, even when there are no large DM substructures present, the clusters contain a small amount of cool ($\sim$1 keV), dense gas. It is likely that this material is spurious, caused by the failure of SPH to mix stripped, low-entropy gas with the hot cluster atmosphere. This requires further investigation so we leave this to future work (but comment on its dependence on resolution in Section 6). In the meantime, we remove the spurious gas following the method suggested by Roncarelli et al. (2013). In this method, discussed further in Appendix A, a small amount of gas with the highest density is excluded from the temperature calculation. In practice, this method also removes the densest, X-ray bright gas in substructures. The outcome is that the X-ray temperatures are much closer to the mass-weighted temperatures for our clusters, so long as the central region is excluded.

2.4 Choice of feedback parameters

The physics of supernova and AGN feedback occur on scales much smaller than are resolvable, so it is unclear how the parameters which govern the amount and manner in which energy is released in a feedback event should be chosen. In order to make this choice, the feedback parameters, $[N_{\rm SN}, T_{\rm SN}, N_{\rm AGN}, T_{\rm AGN}, \epsilon_{\rm f}]$, were varied over a limited range and their effects on the scaling relations and profiles compared.

The supernova feedback parameters ($T_{\rm SN}$ and $N_{\rm SN}$) were varied with the primary intention of matching the cluster gas fractions. As we will see in the next section, supernovae play a particularly important role in keeping most of the cluster baryons in the gas phase. Our default choice of $T_{\rm SN} = 10^7$ K and $N_{\rm SN} = 3$ (also including AGN feedback) produces gas and star fractions that are similar to those observed. Lowering the heating temperature (which corresponds to a lower overall amount of available energy for constant $N_{\rm SN}$ or equivalently the same amount of energy distributed over more particles) results in larger star fractions and lower gas fractions as more gas cools before having a chance to escape from dense regions.

Regarding the AGN feedback parameters, it was found that varying $N_{\rm AGN}$ by an order of magnitude and $\epsilon_{\rm f}$ by a factor of 3 had little effect on the cluster properties. We therefore chose to set $N_{\rm AGN} = 1$, minimizing the period over which energy is stored. When the efficiency is lowered, the accretion rate increases until the amount of heating is able to shut it off. As a result, the amount of energy produced by the BH is similar but the BH mass can be very different. For our work, we chose to keep the default value of $\epsilon_{\rm f} = 0.15$ (Booth & Schaye 2009), which as we will show leads to reasonable BH masses.

The most significant parameter affecting the cluster gas is the AGN heating temperature, $T_{\rm AGN}$. This is highlighted in Fig. 1, where we show scaled pressure (top panels) and entropy (lower panels) profiles for our most massive cluster (left-hand panels) and one of our lowest mass clusters (right-hand panels) at $z = 0$. Within each panel, we show results from two runs, one where we set $T_{\rm AGN} = 10^8$ K (red curve) and one with $T_{\rm AGN} = 10^{8.5}$ K (blue curve). We also show observational data; in the case of the pressure profiles, we show the best-fitting generalized Navarro, Frenk & White (GNFW) models from Planck Collaboration (2013), scaled to the appropriate cluster mass (see Section 4.3). For the entropy profiles, we compare with fits to the REXCESS X-ray data (Pratt et al. 2010).

In the larger mass halo, it is clear that to match the observed pressure profiles in the central region, heating to $T_{\rm AGN} = 10^{8.5}$ K is required; a lower temperature leads to the central region being overpressured. It is also apparent from the entropy profiles that this higher heating temperature is a better match to the observational data outside the inner core ($r > 0.05\,r_{500}$). The importance of the heating temperature can be understood by the fact that heating the gas to a higher temperature allows it to rise further out of the central potential (because the gas will also have higher entropy) and lowers the rate at which its thermal energy is lost to radiative cooling (because the cooling time scales as $\sqrt{T}$ for thermal bremsstrahlung). In the case where the gas is heated to $T_{\rm AGN} = 10^8$ K, the pressure is too high in the central region because the heating is less able to expel gas from the central region, resulting in a denser core.

Looking at the results for the lower mass cluster, it is perhaps unsurprising that setting $T_{\rm AGN} = 10^{8.5}$ K is excessive, creating a pressure profile that is below the observational data and an entropy profile that is too high. Instead, $T_{\rm AGN} = 10^8$ K gives much better results, more similar to the profile for the higher mass halo. Given the order-of-magnitude range in cluster masses, these results suggest that an appropriate heating temperature is that which scales with the virial temperature of the halo (since $T_{\rm vir} \propto M^{2/3}$). We therefore choose to scale $T_{\rm AGN}$ in this way, for all clusters in our sample. Specifically, we use the central mass within each bin and use the above values for the two extremes.

It is unclear whether there is any physical basis for this choice of temperature scaling. It may be that the specific energy in AGN outflows is somehow intimately connected to the properties of the BH (i.e. its mass and/or spin), given that its mass is predicted to be determined by the mass of the DM halo (Booth & Schaye 2010). However, the scaling may also be effectively correcting for the effects of limited numerical resolution, and/or the heating method itself. In the former case, it may be that higher resolution simulations allow the interaction of gas in different phases to be resolved in more detail, which somehow leads to more effective outflows in higher mass clusters (where the cooling time is longer). Alternatively, it may be that if the gas were heated in confined regions (e.g. bubbles), this could naturally produce concentrations of higher entropy gas in higher mass clusters. What is clear is that such fine tuning of the feedback model is still not sufficient to reproduce the entropy profile at all radii (the inner region in particular) although this does

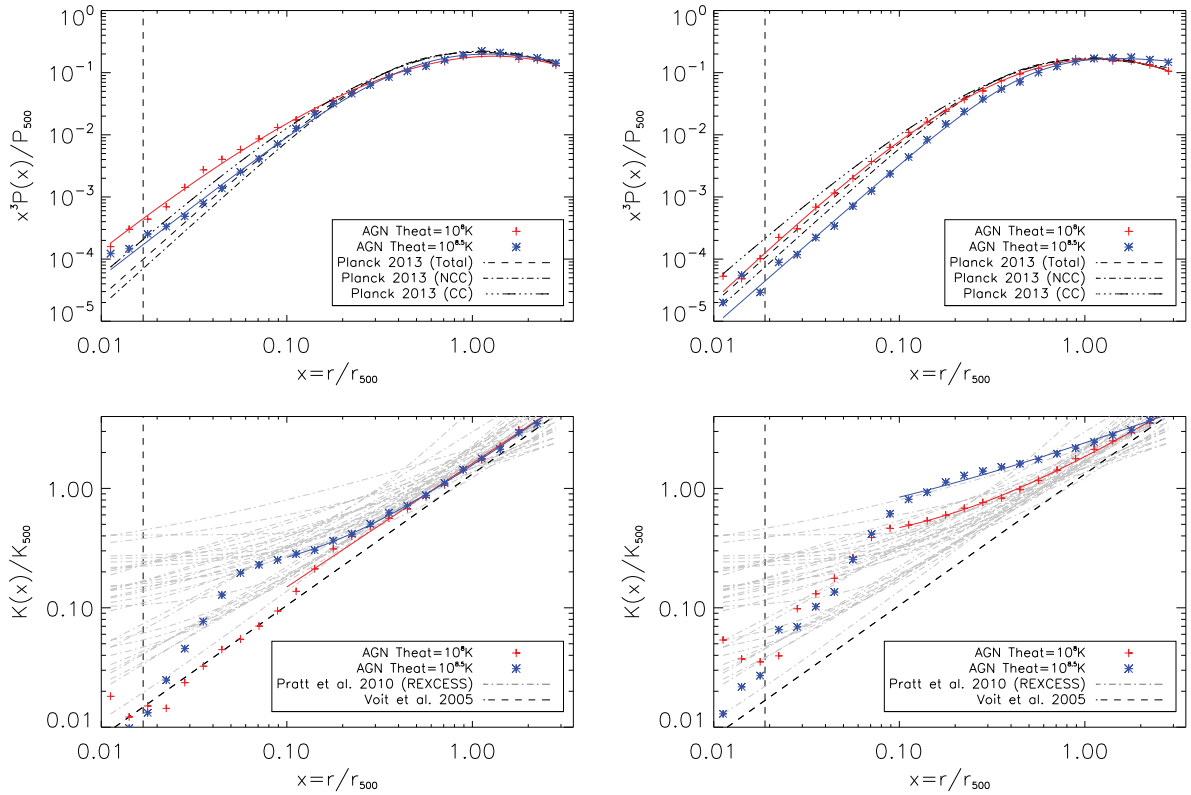

Figure 1. Scaled pressure (top) and entropy (bottom) profiles at $z = 0$, for the most massive ($M_{200} \simeq 10^{15}\,h^{-1}\,\mathrm{M}_\odot$; left) and one of the least massive ($M_{200} \simeq 10^{14}\,h^{-1}\,\mathrm{M}_\odot$; right) clusters. Results shown in red and blue are for runs where $T_{\rm AGN}$ is set to 10^8 and $10^{8.5}$ K, respectively. The pressure profiles are compared to the best-fitting observed profiles from Planck Collaboration (2013), scaled for a cluster with the same mass. In the bottom panels, the grey dot–dashed curves are fits to REXCESS entropy profiles from Pratt et al. (2010), while the black dashed line is the fit to non-radiative clusters in Voit et al. (2005). The vertical dashed line in both panels indicates the gravitational softening radius (2.8 times the equivalent Plummer softening length) where the two-body force deviates from an inverse square law.

improve at higher resolution, as we will show later. Furthermore, the heating temperature could potentially play a role in generating scatter in the entropy profile. We will return to this in Section 4.

3 CLUSTER BARYONS

We now present results for our full sample of 30 clusters, run with our four *physics* models (NR, CSF, SFB and AGN). In this section, we assess the general validity of our AGN model by investigating the overall distribution of cluster baryons. Furthermore, by comparing the different models, we can approximately measure the contribution from individual physical processes (cooling and star formation, supernovae and AGN). We start by comparing the baryon, gas and star fractions with observational data at $z = 0$, before going on to investigate the star formation histories and BH masses.

3.1 Baryon, gas and star fractions

Baryon, gas and stellar fractions, within r_{500}, are shown versus mass for our four simulation sets at $z = 0$, in Fig. 2. We also compare our results with observational data, as detailed in the legends and caption (see also Appendix B).

The baryon fractions (top panel) are similar for the NR and CSF runs and show no dependence on mass. The mean baryon fraction is around 90 per cent of the cosmological value ($\Omega_{\rm b}/\Omega_{\rm m} = 0.15$), similar to previous work (e.g. Crain et al. 2007). Both the SFB and AGN models show more significant (and mass-dependent) depletion, with the AGN model producing values that are closer to the observations. This is due to the feedback expelling some gas from within r_{500} and being more effective at doing so within smaller clusters, which have shallower potential wells.

The middle panel of Fig. 2 displays the hot gas fractions. As expected, the NR results are too high (because radiative cooling is neglected), whilst the CSF values are too low. It is well known that simulations without feedback suffer from the *overcooling* problem, where too much gas is converted into stars (e.g. Balogh et al. 2001). Interestingly, the SFB and AGN runs have similar gas fractions, both of which closely match the observations, with the AGN result having a slightly higher gas fraction. Clearly, the supernova feedback is strong enough by itself to suppress the cooling and star formation in cluster galaxies by about the right amount. As mentioned in the previous section, we tuned the feedback parameters to achieve this result; less effective feedback (e.g. by heating fewer gas particles or using a lower heating temperature) would result in lower gas fractions. The AGN feedback additionally affects the gas in two competing ways. First, as discussed above, it heats the gas more, making it hotter and ejecting some of it beyond r_{500}. Secondly, as the gas is less dense and warmer around the BH particles, star formation is reduced. These two effects partly cancel each other out, with the decreased star formation rate being the slightly stronger effect, resulting in slightly higher gas fractions in the AGN runs.

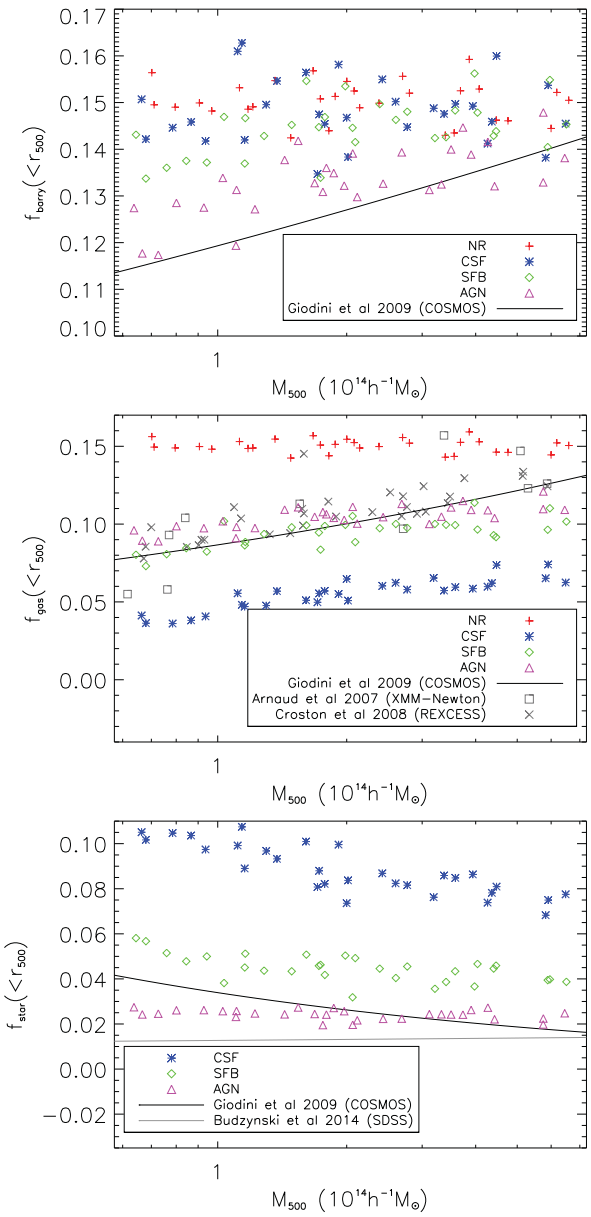

Figure 2. Baryon (top panel), hot gas (middle) and star (bottom) fractions versus halo mass for the four *physics* models at $z = 0$. In all panels, the solid black curve is the best-fitting observed relation from the COSMOS survey (Giodini et al. 2009). We additionally show observed gas fractions from *XMM–Newton* data (Arnaud, Pointecouteau & Pratt 2007; Croston et al. 2008) in the middle panel and the best-fitting relation between star fraction and halo mass from SDSS data (Budzynski et al. 2014) in the lower panel.

Finally, star fractions are presented in the bottom panels of Fig. 2 (the NR results are omitted as these runs do not produce any stars). Again, the CSF runs fail due to overcooling, producing star fractions of the order of 10 per cent. Supernova feedback reduces the fractions by around a factor of 2, but still fail to match the observations. (Recall that we are already close to maximal heating efficiency for a Salpeter IMF; including metal enrichment would likely make the situation even worse). Only when the AGN are included does the star fraction fall to the more reasonable level of 2–3 per cent. The reason for this will now become evident, when we analyse the cluster star formation histories in more detail.

3.2 Formation history and distribution of stars

We now study how the cluster star formation rates are affected by supernova and AGN feedback, by considering the formation times of the stars present in the cluster at $z = 0$. For each object, we identify all star particles within r_{200} and associate them with one of three components: the BCG, the ICL and cluster substructure (SS). For the latter, which we take as a proxy for the cluster galaxies, we identify all star particles belonging to subgroups (as found by SUBFIND) other than the most massive one (i.e. the cluster itself). For the BCG and ICL, we take stars belonging to the most massive subgroup and split them according to their distance from the centre as in Puchwein et al. (2010), who set this demarcation distance to be

$$r_{\rm cut} = 27.3 \left(\frac{M_{200}}{10^{15}\, h^{-1}\, {\rm M}_{\odot}} \right)^{0.29} h^{-1}\,{\rm kpc}. \quad (9)$$

Thus, all stars with $r < r_{\rm cut}$ are assumed to belong to the BCG. While this is a fairly crude method (e.g. one that is more consistent with observations would be to use a surface brightness threshold; e.g. Burke et al. 2012), it nevertheless allows us to assess the effect of feedback in the central region versus the rest of the cluster.

In Fig. 3, we show the stellar mass formed at a given value of a, for stars that end up in each of the three components at $a = 1$, as well as the total stellar mass. From left to right, results are shown for the CSF, SFB and AGN models, respectively. To account for cluster-to-cluster variation, we compute the cumulative star fraction for each object individually, and then present the median curve for the whole sample, multiplied by the median mass at $a = 1$. Ratios of median stellar masses between pairs of runs are summarized in Table 2, for both $a = 0.5$ and 1.

In the CSF runs, more than half the stars have already formed by $a = 0.4$ ($z = 1.5$). Stars in the galaxies (SS) and ICL also tend to have earlier formation times than in the BCG, which continues to form stars steadily until the present, due to the continual accretion of cool gas on to the centre of the cluster. The stellar mass in the BCG is largely unaffected by the introduction of supernova feedback; most of the reduction in stellar mass comes from its effect on the galaxies and ICL. As the ICL is largely stripped material from SS (Puchwein et al. 2010), this is not unexpected. When AGN feedback is included, the largest effect is on the stellar mass of the BCG. Again, this is not surprising as the central BH is significantly more massive than the others and thus provides most of the heating. This is largely why the AGN clusters have lower star fractions than in the SFB model.

The median fraction of stars within each component at $a = 1$ is shown explicitly in Table 3. When feedback is absent (CSF model), nearly half the stars are in satellite galaxies. In the SFB runs, the BCG becomes the largest component as the supernova feedback affects the lower mass haloes. Finally, in the AGN model, the reduction in the BCG mass leads to half of the stars now being in the ICL. Our AGN results compare favourably with Puchwein et al. (2010), who found that ∼50 per cent of stars were in the ICL and ∼10 per cent in the BCG. These results appear to be at odds with some observations of the ICL in clusters (e.g. Gonzalez, Zabludoff & Zaritsky 2005; Gonzalez, Zaritsky & Zabludoff 2007), which tend to find significantly lower fractions. However, more recent work by Budzynski et al. (2014) suggests that the ICL can contribute as much as 40 per cent to the total stellar mass in clusters.

Another issue of current observational interest is the rate at which the BCG grows, primarily due to the recent availability of data for clusters beyond $z = 1$. Lidman et al. (2012) find that the mass of BCGs increases by a factor of 1.8 ± 0.3 between $z = 0.9$ and 0.2.

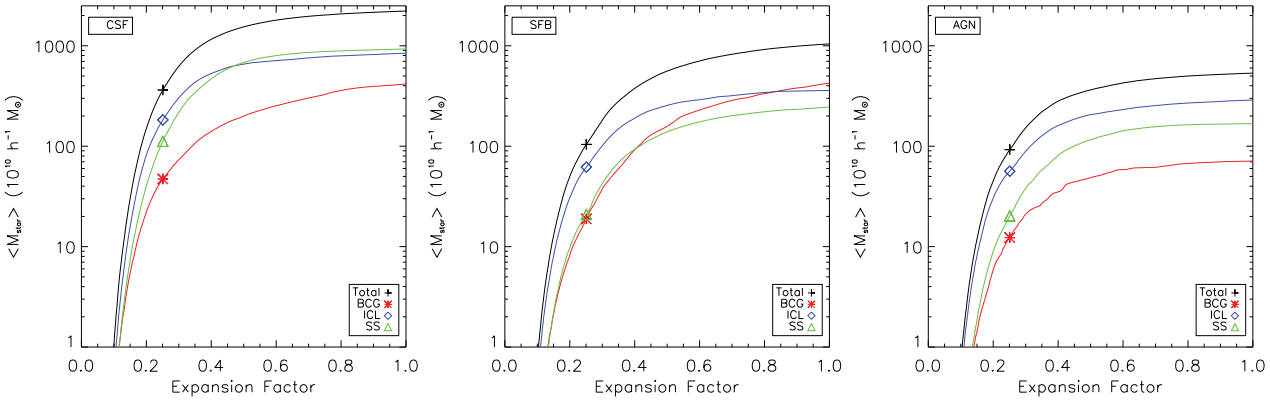

Figure 3. Star formation histories of particles that are within r_{200} at $a = 1$ (black curves), for the CSF (left), SFB (middle) and AGN (right panel) runs. Specifically, the cumulative fraction of stellar mass formed by a given value of a is calculated for each cluster and the median curve is shown, re-scaled to the median final stellar mass. The stars are also sub-divided into where they end up: red curves represent those ending up in the central BCG, blue for those in the ICL and green for those in substructures (galaxies).

Table 2. Comparison of stellar masses formed by $a = 1$ and 0.5, between the CSF, SFB and AGN models, for each of the components that they end up in at $a = 1$.

	$M_{\rm SFB}/M_{\rm CSF}$	$M_{\rm AGN}/M_{\rm CSF}$	$M_{\rm AGN}/M_{\rm SFB}$
$a = 1$			
Total	0.47	0.24	0.50
BCG	0.98	0.16	0.17
ICL	0.45	0.36	0.80
SS	0.26	0.18	0.68
$a = 0.5$			
Total	0.47	0.25	0.53
BCG	0.79	0.19	0.24
ICL	0.34	0.32	0.92
SS	0.30	0.26	0.87

Table 3. Median fraction of stars within the BCG, ICL and SS at $a = 1$, where $M_{\rm T} = M_{\rm BCG} + M_{\rm ICL} + M_{\rm SS}$. The final column lists the fraction of stars in the main subgroup belonging to the ICL, where $M_{\rm SG0} = M_{\rm BCG} + M_{\rm ICL}$.

	$M_{\rm BCG}/M_{\rm T}$	$M_{\rm ICL}/M_{\rm T}$	$M_{\rm SS}/M_{\rm T}$	$M_{\rm ICL}/M_{\rm SG0}$
CSF	0.20	0.34	0.45	0.62
SFB	0.42	0.32	0.25	0.43
AGN	0.14	0.51	0.34	0.78

This is somewhat at odds with the results of Stott et al. (2011), who found that the BCG stellar masses were unchanged at high redshift. By comparing the BCGs in our most massive progenitors at $z = 1$ with our results at $z = 0$, we find that the BCG grows by around a factor of 5, on average, in our AGN model (mainly by dry mergers). This is significantly higher than the observations, even when sample selection is accounted for (Lidman et al. 2012), and requires further investigation. One explanation for these discrepancies is numerical resolution; we will discuss this possibility further in Section 6.

3.3 BH masses

The remaining component in our AGN model clusters is the supermassive BHs. Fig. 4 shows the BH masses within r_{200}, plotted against stellar mass at $z = 0$. We have sub-divided the BHs into those at the cluster centre (red diamonds) and those belonging to cluster

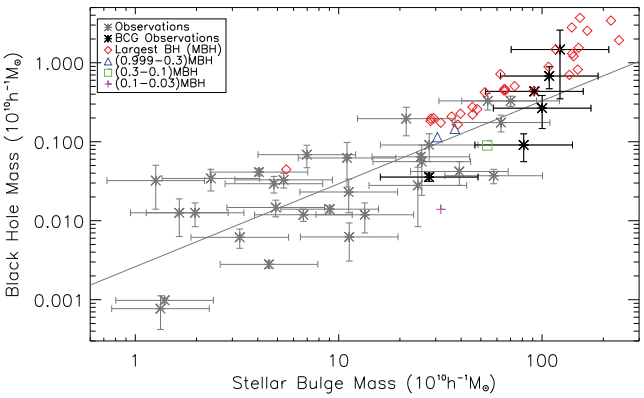

Figure 4. BH mass against stellar mass for our AGN clusters at $z = 0$. Red diamonds are the central and most massive BHs, while the other points correspond to less massive BHs associated with satellite galaxies. Grey and black asterisks are observational data (McConnell & Ma 2013), the latter being objects associated with BCGs.

galaxies with lower masses. The stellar masses are estimated using the crude method outlined above for BCGs (i.e. stars with $r < r_{\rm cut}$). For satellite galaxies, we use the stellar mass in each sub-halo as found by SUBFIND. We also show observational data compiled by McConnell & Ma (2013), highlighting BCGs in bold.

Overall, the simulations are in reasonable agreement with the observational data. As discussed in the previous section, the BH mass can be tuned by varying the heating efficiency, $\epsilon_{\rm f}$. Our default value ($\epsilon_{\rm f} = 0.15$) was found by Booth & Schaye (2009) to reproduce the observed BH mass–stellar bulge mass relation on galaxy scales, so it is somewhat re-assuring that this choice also produces a reasonably good relation for our cluster-scale simulations, given that our results are completely independent from theirs. However, we will show in Section 6 that the position of an individual cluster on this relation depends on resolution.

4 RADIAL PROFILES

In this section, we are principally concerned with how our AGN feedback model affects the spatial distribution of hot gas and stars within our clusters, by considering radial profiles at $z = 0$.

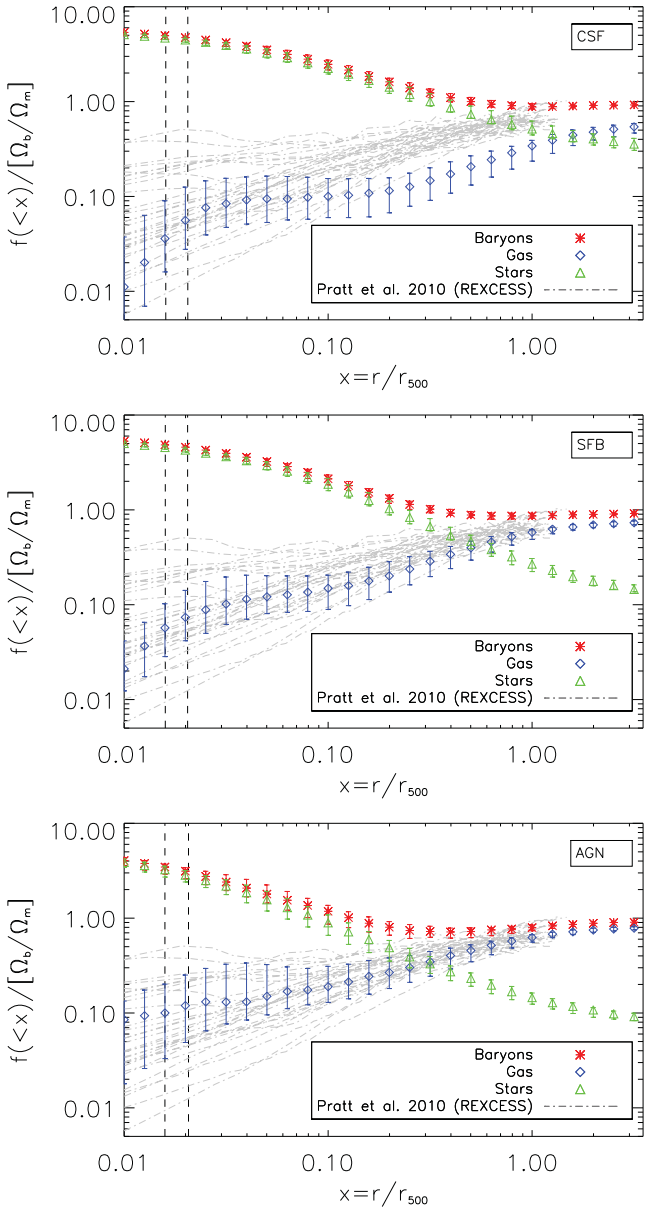

Figure 5. Median baryon (red), hot gas (blue) and star (green) fraction profiles for the cooling and star formation (CSF), supernova feedback (SFB) and AGN feedback (AGN) models at $z = 0$. Error bars indicate the 10th and 90th percentiles, illustrating the cluster-to-cluster scatter within each bin. The vertical dashed lines represent the range in force resolution for the sample. Grey curves are observed gas fraction profiles from REXCESS (Pratt et al. 2010).

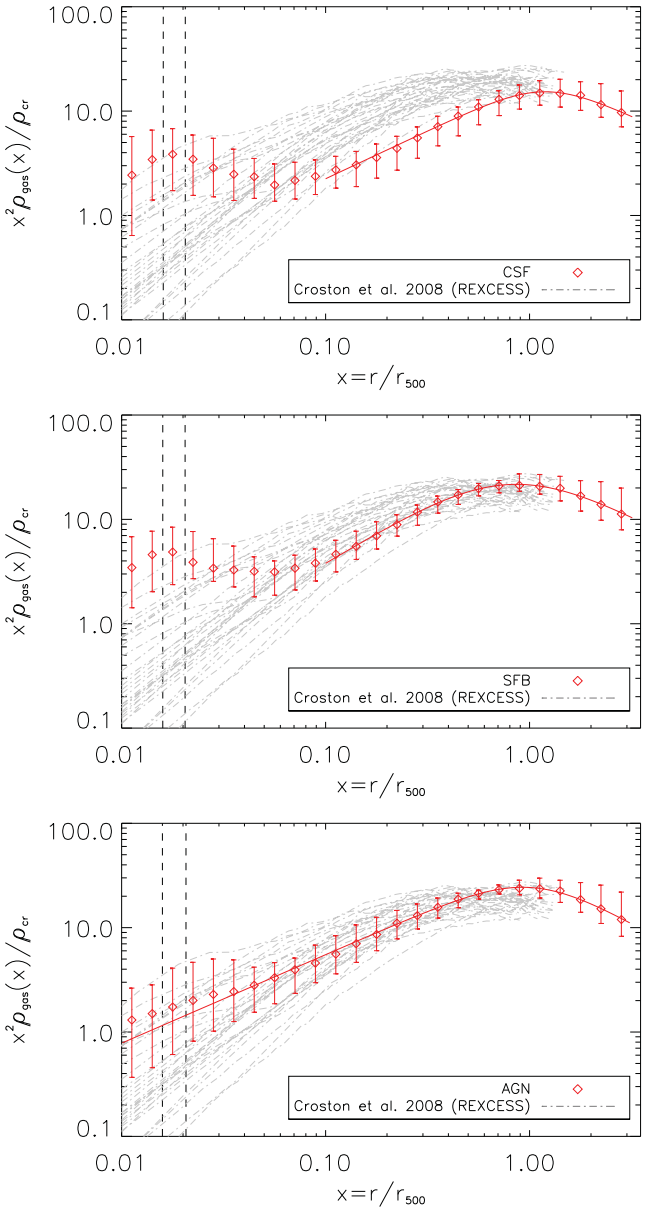

Figure 6. Median gas density profiles for the four sets of runs. The red curve is the best-fitting GNFW model to the median points. The grey lines display observed density profiles from Croston et al. (2008). Other details are as described in Fig. 5.

4.1 Baryon, gas and star fraction profiles

We first consider the radial distribution of baryons, gas and stars. Fig. 5 shows the integrated baryon, gas and star fractions within each radius (plotted as a dimensionless quantity, $x = r/r_{500}$), for our three radiative models (CSF, SFB and AGN). Also plotted are the REXCESS gas fraction profiles (Pratt et al. 2009). For the NR runs (not shown), baryon fractions reach a constant value ($\sim 0.9\Omega_b/\Omega_m$) by $r \simeq 0.2r_{500}$. In the CSF model, the stars dominate at all radii within r_{500}, exceeding the cosmological baryon fraction by a factor of 5 in the centre due to overcooling. In the SFB and AGN runs, the dominance of the stellar component is reduced; for example, the stellar mass only exceeds the gas mass within $\sim 0.3\, r_{500}$ in the AGN clusters. However, the star fraction is still a factor of 4 higher than the cosmological baryon fraction in the centre. Regarding gas fractions, we see that the AGN model best reproduces the observations at all radii, although predicts less scatter in the core.

4.2 Gas density profiles

Gas density profiles are plotted in Fig. 6, along with observed profiles produced by Croston et al. (2008), from the REXCESS data. We multiply the dimensionless density profile (ρ/ρ_{cr}) by x^2 to highlight differences between the models. We also fit the GNFW model (see equation 11 below) to the median points, restricting the fit to outside the cluster core ($0.1 < x < 3$) for the CSF and SFB models.

In accord with the gas fraction profiles, the NR runs (not shown) contain gas that is too dense at all radii within r_{500}, when compared

to observations. Inclusion of radiative cooling and star formation (CSF; top panel) produces a median profile that is too steep in the centre ($x < 0.03$) and too low elsewhere. This is the classic effect of overcooling, where the gas loses pressure support and flows into the centre before finally being able to cool down sufficiently to form stars. (Note the effect is not as clear for the integrated gas fraction due to the large increase in stellar mass which dominates the total mass in the centre.) When supernova feedback is included (SFB; middle panel), the effect of the supernovae is to raise the gas density in the cluster as the feedback keeps more of the gas in the hot phase. The result is a gas density profile that matches observations reasonably well beyond the core ($x > 0.1$) but the central densities are still too high. This problem is largely solved by the inclusion of AGN feedback, which heats the core gas to much higher temperatures ($T \geq 10^8$ K), allowing more gas to move out to larger radii. As a result, the agreement between the AGN model and the observations is better, although the median profile is a little steep in the centre. This agreement is not too surprising, given that our AGN feedback model was tuned to match the observed median pressure profile (see below).

We also checked if the density profiles depend on mass. To do this, we first ranked the clusters in mass and then divided the ranked list into three bins of 10 objects, before comparing the median profile for each mass bin. In all three radiative models, we find a small but significant trend such that higher mass clusters have scaled density profiles with higher normalization. As a result, the scaled entropy profiles of the higher mass objects are lower (but no such trend is seen for the pressure profiles). This is expected given the mass-dependent effects of cooling and feedback on the gas fraction (as shown in Fig. 2).

4.3 Pressure profiles

It is also useful to study pressure profiles, as the pressure gradient provides hydrostatic support in the cluster. Furthermore, the pressure profile allows us to understand any changes in the SZ effect, as the Y parameter can be expressed as the following integral of the pressure profile for a spherically symmetric cluster

$$D_{\rm A}^2 Y_{\rm SZ} = \frac{\sigma_{\rm T} r_{500}^3}{m_{\rm e} c^2} \int_0^1 P_{\rm e}(x)\, 4\pi x^3\, {\rm d}\ln x, \tag{10}$$

where $P_{\rm e} = n_{\rm e} k T_{\rm e}$ is the pressure from free electrons (assumed to be proportional to the hot gas pressure). Plotting $x^3 P(x)$ therefore allows us to assess the contribution to $Y_{\rm SZ}$ from the gas (and therefore its total thermal energy) from each logarithmic radial bin.

In Fig. 7, we show dimensionless pressure profiles (scaled to P_{500}; see Appendix A) for our three radiative models at $z = 0$. The median data points are fitted with the GNFW model (e.g. Arnaud et al. 2010), defined as

$$\frac{P}{P_{500}} = \frac{P_0}{u^\gamma (1 + u^\alpha)^{(\beta-\gamma)/\alpha}}, \tag{11}$$

where $u = c_{500}\, x$, c_{500} is the concentration parameter, P_0 is the normalization and $[\alpha, \beta, \gamma]$ are parameters that govern the shape of the profile. This allows us to make a direct comparison with the best-fitting GNFW models for the *Planck* SZ cluster sample (we show results for their total sample, cool-core clusters and non-cool-core clusters; Planck Collaboration 2013). Note that the normalization of the observed pressure profiles, P_0, exhibits a weak dependence on mass (Arnaud et al. 2010), which can be summarized as follows:

$$P_0(M_{500}) = P_3 \left(\frac{M_{500}}{3 \times 10^{14}\, {\rm M}_\odot} \right)^{0.12}, \tag{12}$$

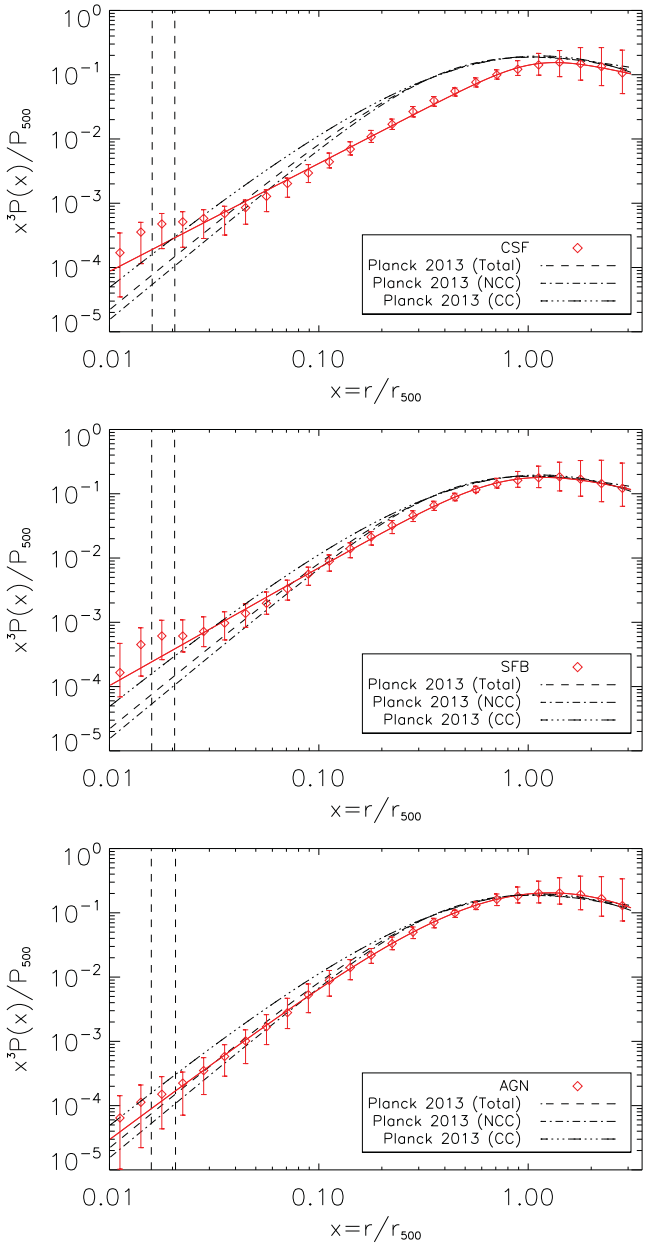

Figure 7. Dimensionless pressure profiles for the three radiative models at $z = 0$. The red curve is the best-fitting GNFW model to the median points. Observational fits are also displayed for the cool core, non-cool core and total median profiles from Planck Collaboration (2013). Other details are as described in Fig. 5.

where P_3 is a free parameter that equals P_0 when $M_{500} = 3 \times 10^{14}\, {\rm M}_\odot$. For our full sample presented here, we use equation (12) to re-scale the profiles for individual clusters before fitting the GNFW model to our median profile and comparing with the observed fits for $P_0 = P_3$.

It is immediately apparent that the largest contribution to $Y_{\rm SZ}$ occurs around r_{500}, far away from the complex physics in the cluster core (Kay et al. 2012). At these large radii, there is only a small increase in the pressure when going from CSF→SFB→AGN, suggesting that the $Y_{\rm SZ}$ parameter is reasonably insensitive to the physical model used. However, the contribution from regions with $r < r_{500}$ cannot be ignored, especially when comparing CSF to SFB/AGN (as we shall see in the next section, this leads to

significant differences in the Y_{SZ}–M_{500} relation between these models). The differences in pressure profiles between the runs are largely similar to those seen for the gas density profile; this is because the density is a much more sensitive function of radius (varying by orders of magnitude) than the cluster temperature. By design, the AGN model provides a good match to the observed data. In detail, it still underestimates the pressure slightly (cf. the *Planck* total profile) except in the very centre (where the gas is unresolved at $r < 0.02\,r_{500}$) and at the largest radii ($r > r_{500}$).

4.4 Spectroscopic-like temperature profiles

Projected spectroscopic-like temperature profiles are shown in Fig. 8, in comparison with observational results from Leccardi & Molendi (2008). As discussed in Section 2, we calculated T_{sl} by excluding a very small amount of gas with the highest density within each bin (Roncarelli et al. 2013). Failure to do this results in noisier profiles but does not significantly affect the normalization (since the profiles are divided by an average temperature).

All models predict profiles with a qualitatively similar shape, where the temperature declines towards the centre and at large radii. This shape reflects the underlying gravitational potential (because the gas is approximately in hydrostatic equilibrium). Comparing the models with the observations in detail, the NR results (not shown) are very similar at all radii, except in the very centre ($r < 0.1 r_{180}$) where the observed gas is relatively cooler. The CSF and SFB models predict lower central temperatures but the profiles have a much higher peak temperature than observed. Again, this is due to cooling: as higher entropy gas flows inwards, it is adiabatically compressed, as can also be seen from the flattening of the entropy profile (see also Tornatore et al. 2003; Borgani et al. 2004). The inclusion of AGN feedback has a more pronounced effect on shape of the inner temperature profile, reducing the peak value and the temperature gradient of the gas around it. This result, while a closer match to the observational data, may be due to the feedback not acting on enough of the gas in the core (see below).

4.5 Entropy profiles

Entropy profiles show directly the effects of non-adiabatic heating (from feedback, which increases the entropy) and radiative cooling (which decreases the entropy). Fig. 9 shows dimensionless entropy (K/K_{500}) profiles for our simulated clusters. As a guide to the eye, we fit the median data points at $x > 0.1$ with the function, $K(x) = K_0 + K_{100}x^{\alpha}$ (shown as the red curve), where $x = r/r_{500}$ and $[K_0, K_{100}, \alpha]$ are free parameters. We also show similar fits to observational data from the REXCESS sample (Pratt et al. 2010) and the power-law profile derived from non-radiative simulations by Voit et al. (2005), re-scaled for $\Delta = 500$ (assuming a baryon fraction $f_b = 0.15$ and a value $r_{500}/r_{200} = 0.659$, as derived from an NFW profile with concentration $c_{500} = 3.2$, following Pratt et al. 2010).

The NR model (not shown) reproduces the Voit et al. (2005) relation very well, predicting a power-law entropy profile at all resolved radii as expected. This result is below the observational data, owing to the gas density being too high. The entropy profiles in the CSF model show a distinctly different shape: a sharp rise in entropy with radius until $r = 0.1$–$0.2\,r_{500}$, where it reaches a plateau, before rising more gently at larger radius. This shape, at odds with the observations, can be understood as follows. As the innermost gas cools and flows towards the centre, higher entropy gas from larger distances flows in to replace it, creating the excess

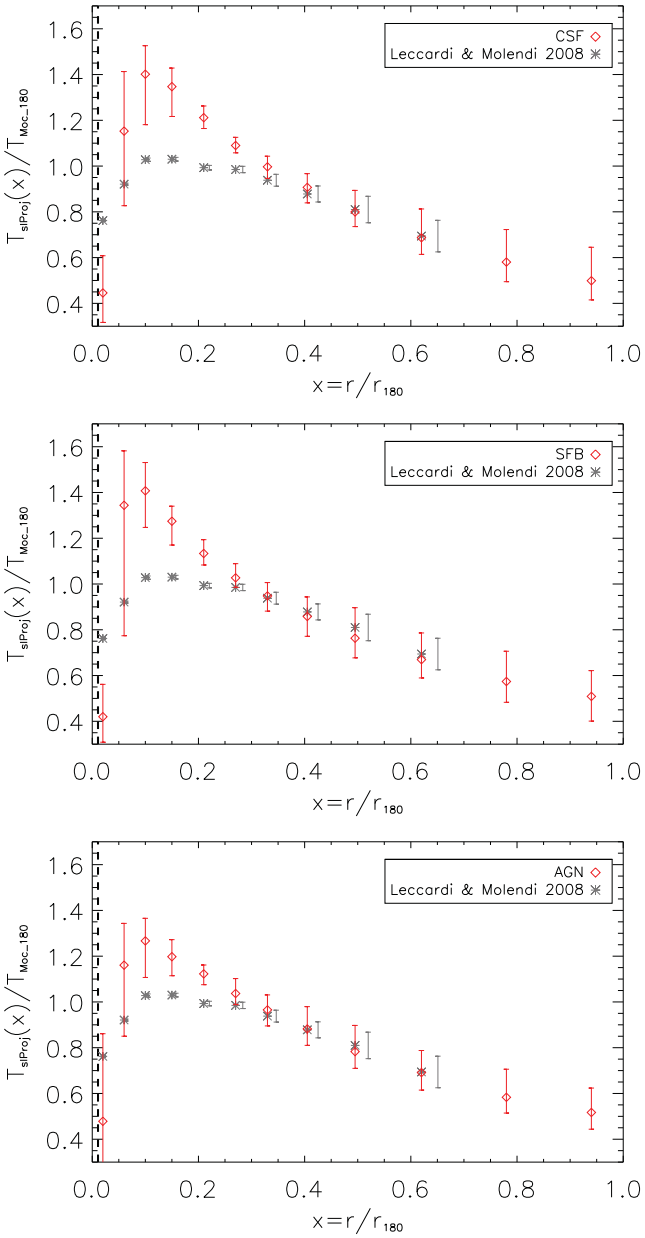

Figure 8. Projected spectroscopic-like temperature profiles for the three radiative models at $z = 0$. In this case, radii are scaled to r_{180} and the temperature in each bin is divided by the average value across the range, $0.1 < r/r_{180} < 0.7$. Grey stars represent the observational data from Leccardi & Molendi (2008) where the profiles are presented in a similar way. Other details are as described in Fig. 5.

in entropy (more than required by the observational data) outside the core. At smaller radii, the cooling time becomes sufficiently short (compared to the local dynamical time) that the gas rapidly loses energy, creating a steep decline in entropy towards the centre of the cluster. The generation of excess entropy in simulations with cooling has been seen in many previous studies (e.g. Muanwong et al. 2001; Borgani et al. 2002; Davé et al. 2002).

Supernova feedback increases the gas density (and pressure) throughout the cluster, reducing the effects of cooling and lowering the entropy profile outside the core, bringing the results into reasonable agreement with the observational data. However, the steep decline within the core is still evident as the supernovae are

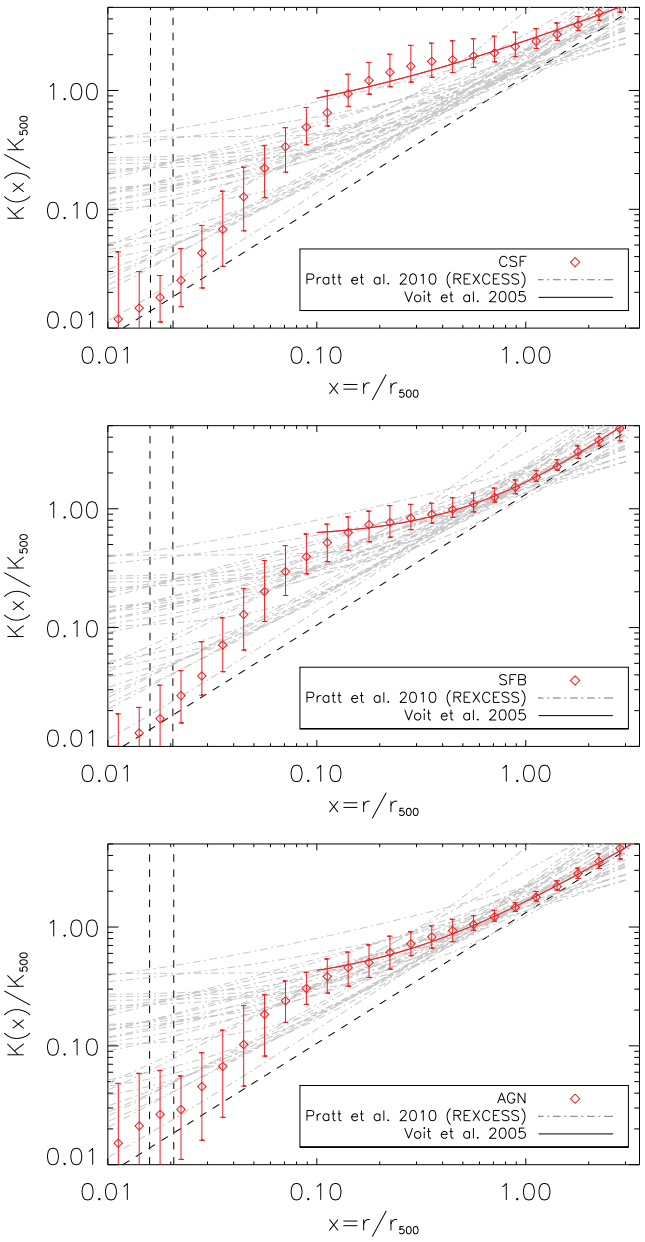

Figure 9. Dimensionless entropy profiles for the three radiative models at $z = 0$. Red curves are model fits to the median data points outside the core region ($x > 0.1$; see the text for details). Grey curves are similar fits to observed X-ray clusters from the REXCESS sample, presented in Pratt et al. (2010). The dashed black line is the profile derived from non-radiative simulations by Voit et al. (2005), re-scaled for $\Delta = 500$. Other details are as described in Fig. 5.

unable to provide sufficient energy to offset the cooling that is going on there. The situation is partially improved when AGN feedback is included, where the inner entropy profile is now similar to that of cool-core clusters. However, the characteristic break at $r \simeq 0.1\, r_{500}$ is still present.

As was discussed in Section 2, the AGN heating temperature was tuned to provide approximately the correct level of heating across the cluster mass range (as required by matching the pressure profile). However, as the simulations do not match the observed entropy profile shape in detail (and the scatter), it is likely that there is still something wrong, or incomplete, with our method.

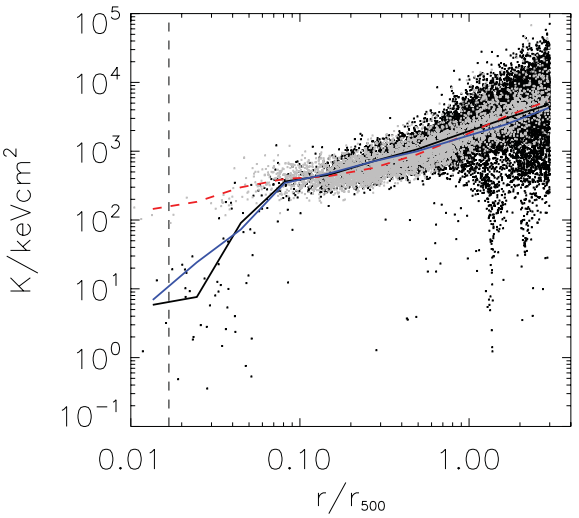

Figure 10. Entropy versus radius for a random subset of hot gas particles (black points) in our most massive cluster at $z = 0$, run with the AGN model. The light grey points are a subset of particles directly heated by an AGN. The black solid, blue solid and dashed lines are binned median profiles for all, SN-heated and AGN-heated particles, respectively.

To gain some insight into the origin of this discrepancy, we show the entropy of a subset of individual gas particles versus radius for our most massive cluster at $z = 0$ (black points), in Fig. 10. As expected, the median profile (solid line) for all gas particles is very similar to that for the whole cluster sample and the break is clearly present around $r = 0.08\, r_{500}$. The blue solid curve is the profile for the subset of gas particles that were directly heated by supernovae (these make up around 20 per cent of the gas within $3\, r_{500}$, the maximum radius shown). Clearly, the two profiles are very similar, as is also the case for AGN-heated particles (light grey points and dashed curve) beyond the break, which make up only 3 per cent of the gas. This shows that most of the heated particles (from both SNe and AGN) are well mixed with the other gas throughout most of the cluster. Within the central region, however, the AGN-heated gas particles are much hotter and thus have much higher entropy ($K \sim 100\,\mathrm{keV\,cm^2}$) than the rest of the gas (this is the expected level given the typical density, $n_\mathrm{H} \simeq 0.1\,\mathrm{cm^{-3}}$, of the material, which is being heated to a temperature, $T_\mathrm{AGN} = 10^{8.5}$ K). Nevertheless, the average entropy in the core is dominated by the cooler gas and so the break persists. We also note that a similar profile shape was found by McCarthy et al. (2010) on group scales (see their fig. 1). This is not surprising since we are effectively using the same AGN feedback model as theirs.

One possible resolution to the problem is to include some degree of entropy mixing in the simulation. It is well known that standard SPH algorithms suppress gas mixing e.g. via the Kelvin–Helmholtz instability (see Power, Read & Hobbs 2014 for recent work). Additionally, explicitly including thermal conduction may help (Voit et al. 2008). Discreteness effects from having relatively poor numerical resolution may also play a part; as we show in Section 6, runs with higher spatial resolution produce smoother profiles. Such issues will be investigated in future work.

We are also interested in *when* the feedback happens. In McCarthy et al. (2011), they argue that the AGN feedback largely works in their groups by *ejecting* gas from galactic-scale haloes at high redshift ($2 < z < 4$). Again, focusing on our highest mass cluster, we find that nearly all the AGN feedback energy is released at low redshift ($z < 1$) because that is when most of the BH growth occurs (see

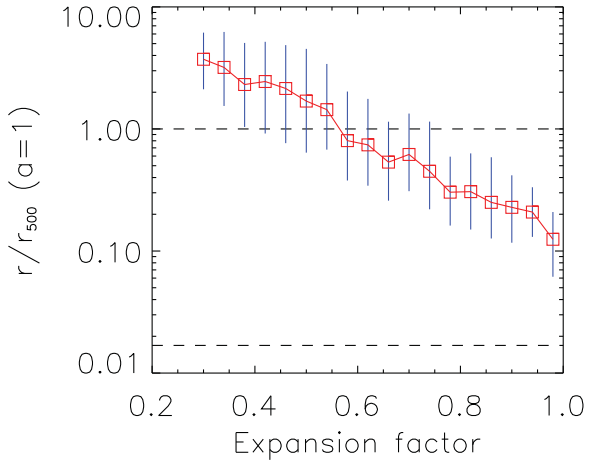

Figure 11. Final radius of AGN-heated particles (in r_{500} units) versus the value of a when they were first heated, for the most massive cluster. Squares are median values while the vertical lines indicate the 10th and 90th percentiles. The horizontal dashed lines indicate r_{500} and the softening scale.

Section 6, Fig. 15). A plausible explanation for this difference is that it is harder for a BH to significantly influence its surrounding environment in a cluster, where the potential is much deeper, and we have therefore crossed the transition from a feedback-dominated regime to a cooling-dominated regime (as argued by Stott et al. 2012). The cooling gas in the core (which as we saw above does not appear to get too disturbed by the AGN-heated gas) then continues to feed the BH, leading to significant growth at late times. (This can be true even when the accretion rate is small compared with the Eddington rate because the Bondi–Hoyle rate $\dot{M} \propto M_{\rm BH}^2$.) As a result of this late heating, most of the heated gas remains in the cluster by $z = 0$, while only gas that is heated earliest ends up beyond r_{500}. We confirm this in Fig. 11, where we plot the final radius of the heated particles versus the time when they were first heated (we additionally restricted our sample to those particles that were within $0.5\,r_{500}$ in the NR run, to approximately select those particles that were heated by the central BH). There is a strong negative correlation, with gas heated at $a > 0.6$ largely remaining inside the cluster. (Heating the gas to a lower temperature reduces the final radius at fixed a, as would be expected.)

5 SCALING RELATIONS

While profiles help us to understand the interplay of different physical effects within the clusters, they do not easily describe their global properties and how they scale with mass. Scaling relations do this, as well as providing additional, important observational tests of the models. Furthermore, observable-mass scaling relations are an important part of cosmological analyses that use clusters. The primary aim of this section will therefore be to investigate how key observable scaling relations ($Y_{\rm SZ}$, $L_{\rm bol}$ and $T_{\rm sl}$ versus M_{500}) vary as we add increasingly realistic physics. We also compare our results at $z = 0$ with observational determinations, although stress that such a comparison is not rigorous as we do not measure the properties in exactly the same way (importantly, we do not investigate the effects of hydrostatic mass bias in this paper, which is likely to lead to a small increase in the normalization of our scaling relations owing to the hydrostatic masses being lower than the true masses).

We will also investigate how our models differ when the redshift evolution of the scaling relations is considered; for this, we take the most massive progenitor of each cluster so our sample contains 30 objects at all redshifts. While our results should be interpreted with some caution given that we are not comparing mass-limited samples at each redshift (or indeed, flux-limited samples), they are still useful for comparing the relative importance of the different physical processes.

Table 4. Fit parameters for the scaling relations at $z = 0$. Column 1 lists the relation and model; while columns 2–7 give the best-fitting values for the normalization (A), slope (B) and intrinsic scatter (S), together with their uncertainties (σ), estimated using the bootstrap method. The quantities $T_{\rm sl,\,OC}$ and $L_{\rm bol,\,OC}$ are for when gas from within the core ($r < 0.15\,r_{500}$) is omitted.

Run	A	$\sigma_{\rm A}$	B	$\sigma_{\rm B}$	S	$\sigma_{\rm S}$
$Y_{\rm SZ}$–M_{500}						
NR	−5.588	0.005	1.66	0.01	0.027	0.004
CSF	−5.923	0.013	1.85	0.03	0.047	0.006
SFB	−5.697	0.009	1.71	0.02	0.032	0.004
AGN	−5.653	0.008	1.70	0.02	0.034	0.004
$T_{\rm sl}$–M_{500}						
NR	0.204	0.016	0.61	0.03	0.062	0.010
CSF	0.126	0.009	0.30	0.03	0.047	0.007
SFB	0.120	0.014	0.27	0.04	0.057	0.010
AGN	0.296	0.013	0.25	0.05	0.082	0.010
$T_{\rm sl,\,OC}$–M_{500}						
NR	0.223	0.012	0.64	0.03	0.052	0.006
CSF	0.409	0.005	0.60	0.01	0.024	0.003
SFB	0.361	0.006	0.60	0.01	0.026	0.003
AGN	0.354	0.005	0.60	0.01	0.021	0.002
$L_{\rm bol}$–M_{500}						
NR	0.517	0.048	0.97	0.09	0.179	0.024
CSF	−0.151	0.038	1.79	0.09	0.159	0.024
SFB	0.309	0.034	1.46	0.08	0.138	0.016
AGN	−0.158	0.027	1.54	0.06	0.123	0.019
$L_{\rm bol,\,OC}$–M_{500}						
NR	0.167	0.038	1.08	0.07	0.124	0.028
CSF	−1.070	0.075	1.73	0.16	0.240	0.035
SFB	−0.434	0.090	1.35	0.17	0.255	0.051
AGN	−0.432	0.036	1.45	0.08	0.113	0.032

All scaling relations are fitted with a power-law model

$$E(z)^{\gamma} C_{500} = 10^{\rm A} (M_{500}/10^{14}\,h^{-1}\,{\rm M}_{\odot})^{\rm B}, \quad (13)$$

where $E(z) = H(z)/H_0$ and C_{500} is the observable, which can take the form of $Y_{\rm SZ}$, $L_{\rm bol}$ or $T_{\rm sl}$, with all properties measured within r_{500}. We allow both the normalization, A, and index, B, to vary when performing a least-squares fit to the set of data points, ($\log_{10}C_{500}$, $\log_{10}M_{500}$). We fix the parameter, γ, to the self-similar value when studying scaling relations at $z > 0$: for ($Y_{\rm SZ}$, $L_{\rm bol}$, $T_{\rm sl}$), these values are $\gamma = (-2/3, -7/3, -2/3)$, respectively. We also estimate the intrinsic scatter in each relation using

$$S = \sqrt{\frac{1}{N-2}\sum_{i=1}^{N}\left[\log_{10} C_i(M_i) - \log_{10} C_{500}(M_i)\right]^2}, \quad (14)$$

where $N = 30$ is the number of clusters in our sample, C_i is the value being measured for the ith cluster with mass, M_i, and C_{500} is the best-fitting value at the same mass. Uncertainties in A, B and S are estimated using the bootstrap method, re-sampling 10 000 times and computing the standard deviation of the distribution of best-fitting values. Results for the fits at $z = 0$ are summarized in Table 4 and we discuss each relation in turn (including the evolution of the parameters with redshift), below.

5.1 The Y_{SZ}–M_{500} relation

The Y_{SZ}–M_{500} relation is a good basic test, given that Y_{SZ} is proportional to the total thermal energy of the intracluster gas. Unlike X-ray luminosity, it should be relatively insensitive to non-gravitational physics, a result confirmed with previous simulations (e.g. da Silva et al. 2004; Nagai 2006; Battaglia et al. 2012; Kay et al. 2012).

In the top panel of Fig. 12 the Y_{SZ}–M_{500} relation at $z = 0$ is plotted, where red crosses, blue stars, green diamonds and purple triangles are results from the NR, CSF, SFB and AGN runs, respectively. We also show the best-fitting relations to each data set as solid lines with the same colour as the data points. As an observational comparison, the best-fitting straight line to *Planck* and *XMM–Newton* data (Planck Collaboration 2011) is also plotted in black.

As expected, the Y_{SZ}–M_{500} relation is well defined for all the runs with minimal scatter ($S < 0.05$), but it is immediately apparent that the CSF relation is a poor match to the observations, whereas the NR, SFB and AGN runs all do reasonably well (the normalization agrees to within 10–20 per cent and may be improved once the effect of hydrostatic mass bias is accounted for). The severe overcooling present in the CSF run leads to a reduction in Y_{SZ} as the gas cools and provides less pressure support. While the NR model is unable to reproduce many other observables, the result here is a good match to the observations, suggesting that the feedback must be strong enough to counteract cooling without increasing the thermal energy significantly (as also seen with the temperature profiles). The similarity between the SFB and AGN runs can be explained by the fact that the dominant contribution to Y_{SZ} occurs at $r \simeq r_{500}$. In this region, the feedback from supernovae is more effective than from AGN, but this conclusion may at least in part be affected by our method for incorporating BHs within the simulation. Nevertheless, it emphasizes the point that the mitigation of cooling by supernovae in clusters is an important factor.

We have also examined the dependence of the fit parameters (A and B) on redshift; the lower panels in Fig. 12 show results for the normalization, A, and slope, B, from each snapshot to $z = 1.4$. In all models except CSF, the normalization evolves in accord with the self-similar scenario (the small amount of drift at higher redshift is due to changes in the gas temperature, as discussed below). The amount of overcooling in the CSF runs (which reduces the gas density) becomes more severe with time, leading to a normalization that is around 70 per cent of the observed value at $z = 1.4$ and 50 per cent at $z = 0$. The slope exhibits significantly more scatter between redshifts than the normalization, but there is still a clear difference between CSF and the other models.

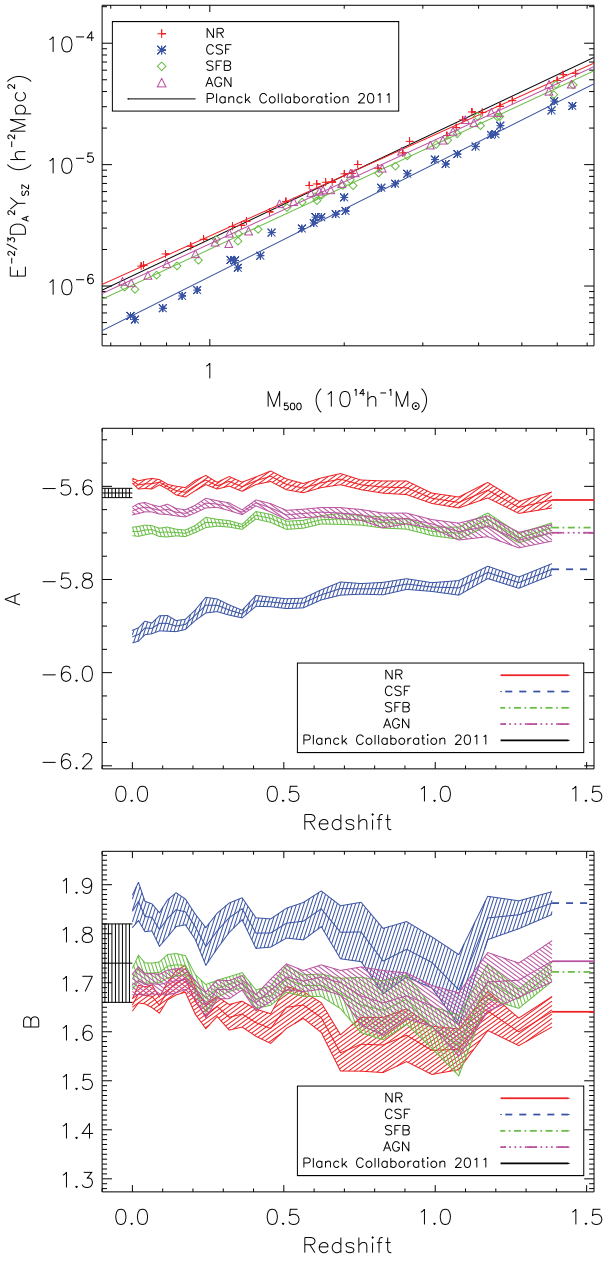

Figure 12. Y_{SZ}–M_{500} relation at $z = 0$ (top panel) for the non-radiative (NR; red crosses), cooling and star formation (CSF; blue stars), supernova feedback (SFB; green diamonds) and AGN (magenta triangles) models, respectively. Accompanying solid lines are best-fitting power laws to the data, while the observed relation from Planck Collaboration (2011) is also plotted as a black line. The middle and bottom panels show the evolution of the normalization and slope with redshift where the shaded region illustrates the uncertainty in each parameter (one standard deviation from the best-fitting values of A and B). The black line and shaded region represent the best-fitting value and error from observations of low-redshift clusters (Planck Collaboration 2011).

5.2 The T_{sl}–M_{500} relation

Spectroscopic-like temperature versus mass relations are displayed in Fig. 13, where T_{sl} is calculated after the densest gas is removed from each shell (Roncarelli et al. 2013). The top panels show results at $z = 0$; in the right-hand panel, the core region ($r < 0.15\,r_{500}$) was excluded from the temperature calculation. We also show observational results from the REXCESS sample (Pratt et al. 2009).

None of the models match the observational data when the temperature is measured using all gas within r_{500}. The NR clusters have temperatures that are around 60 per cent of the observational values, with a slope ($B = 0.61$) that is closest to the self-similar value ($B = 2/3$). Including supernova feedback makes little difference to the temperature; only AGN feedback produces a significant increase, with the temperature being around 75 per cent of the observed temperature at fixed mass. However, the slope for the AGN model (and the other radiative models) is considerably flatter than the self-similar prediction. This is because the more massive clusters have significantly higher fractions of cooler gas in the core that is still hot enough ($kT > 0.5$ keV) to be included in the T_{sl} calculation.

When the core is excluded, the NR results change very little at $z = 0$ but the runs with cooling all predict temperatures that are closer to the observational data (80–90 per cent of the observed

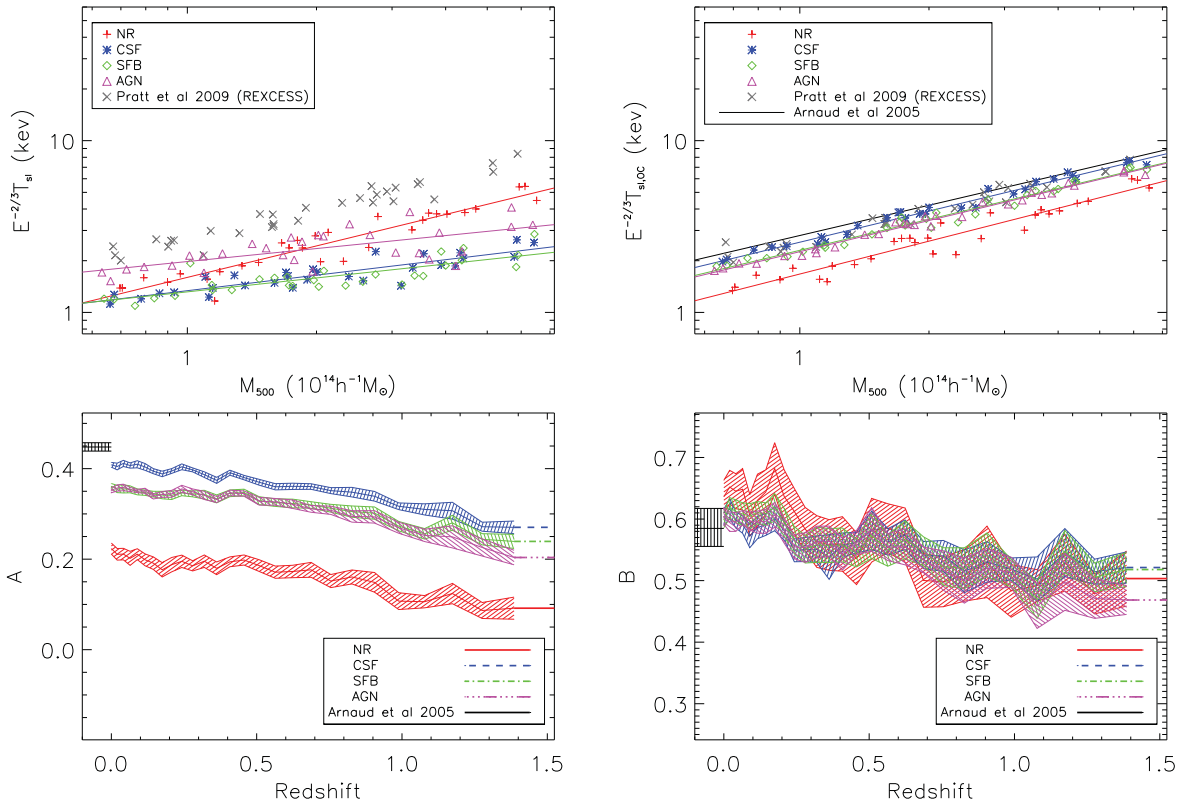

Figure 13. T_{sl}–M_{500} scaling relations for the NR, CSF, SFB and AGN models at $z = 0$ (top panels), when the core is included (top-left) and excluded (top-right) from the temperature calculation. The bottom panels show the dependence of the normalization and slope parameters with redshift, when the core region is omitted. Grey crosses and the black line/shaded region are observational results from Pratt et al. (2009) and Arnaud, Pointecouteau & Pratt (2005), respectively. All other details are as used in Fig. 12.

values at fixed mass). While the CSF and SFB runs show the largest change (where feedback is absent and ineffective in the core, for the respective runs), an improved match is also seen for the AGN model. Furthermore, all models have a slope close to the self-similar model at $z = 0$, varying from ∼0.6 for the AGN model to 0.7 for the SFB model; the AGN model is closest to the observational data ($B = 0.58$).

Studying the results at higher redshift, we find that the normalization evolves negatively with redshift in all models, regardless of whether the core is included or not (results for the latter case are shown in the bottom panels of Fig. 13). We also checked the mass-weighted temperature–mass relation and a similar result was found, suggesting that the result may be peculiar to the way in which our clusters were selected (larger, mass-limited samples would be required to check this). For the slope, when the core is included the lower values seen in the radiative models persist to high redshift, while the non-radiative value decreases slightly. When the core is excluded, all models exhibit similar behaviour (again, this is seen when considering the mass-weighted temperature).

5.3 The L_{bol}–M_{500} relation

Finally, results from X-ray luminosity scaling relations are displayed in Fig. 14. The panels on the left are for all emission within r_{500} and the right when the core ($0.15\,r_{500}$) is excluded. Results from each simulation model are shown as before and we also show observational data points from REXCESS (Pratt et al. 2009; grey crosses).

As expected, clusters in the NR model are overluminous, both with and without the core, due to the fact that the gas is too dense at all radii. The slope ($B = 0.97 \pm 0.09$) is flatter than the self-similar value ($B = 4/3$). While part of this discrepancy could be due to sample selection given the large intrinsic scatter ($S = 0.18 \pm 0.02$), the main reason is that the lower mass clusters are sufficiently cold ($kT \sim$ 1–3 keV) that line emission makes a significant contribution to the luminosity (the cooling function is approximately constant at these temperatures, for $Z = 0.3\,Z_{\odot}$).

In the CSF run, cooling causes a significant drop in luminosity, driven primarily by the decrease in density as the gas cools below $T = 10^5$ K and forms stars. It is interesting that the results match the observations reasonably well when all emission is included, but the CSF clusters are underluminous when the core is excluded. Again, the former result is well known (e.g. Bryan 2000; Muanwong et al. 2001), being due to the effect of cooling removing the dense, low-entropy gas. However, this effect produces density (or entropy) profiles with the wrong shape: the density is too low beyond the core and too high in the centre. This leads to the core-excluded relation being too low.

Supernova feedback increases the density of the gas within r_{500} due to reduced star formation, resulting in a luminosity profile that is higher than for CSF across the whole radial range. This leads to a luminosity that is also too high inside the core (due to the supernovae being ineffective at suppressing the cooling there) but matches the observed luminosities if the core is excluded. Finally, when AGN feedback is included, the density and therefore luminosity in the central region is reduced as gas is expelled, but this has a lesser

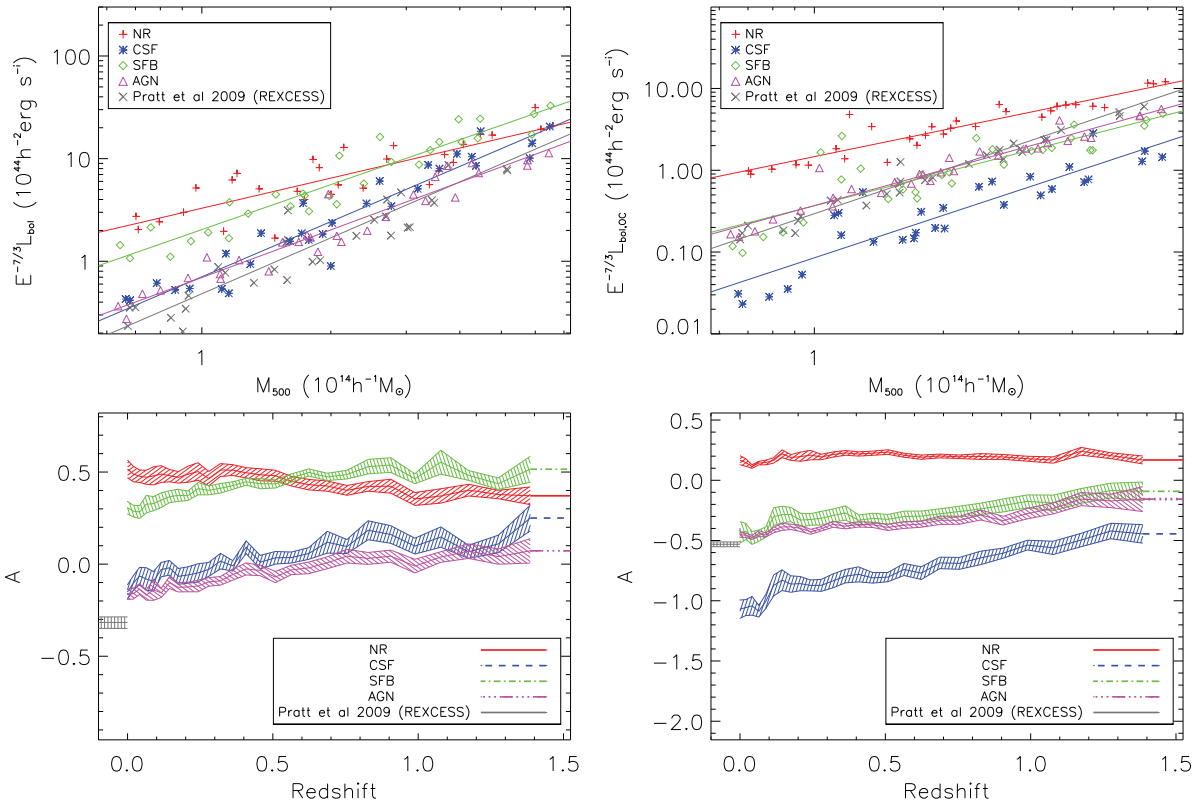

Figure 14. L_{bol}–M_{500} scaling relations for the NR, CSF, SFB and AGN models at $z = 0$ (top panels) and evolution of the normalization with redshift (bottom panels). Panels on the left (right) show results when luminosities are calculated including (excluding) the core region. Grey crosses/line/shaded region are observational results from REXCESS (Pratt et al. 2009). All other details are as used in Fig. 12.

effect on the outskirts. Thus, the AGN relation provides a better match to the observed mean relation in both cases.

The intrinsic scatter in the L_{bol}–M_{500} relation is similar to the REXCESS observations (0.17) for the NR and CSF runs, but is too small in the AGN model ($S = 0.12 \pm 0.02$). This again points to the fact that, in our most realistic model, the full range of cool-core and non-cool-core clusters is not recovered. When the core is excised, the scatter decreases in the NR and AGN cases, but actually increases in the CSF and SFB runs. Closer inspection reveals that this is due to a few objects with unusually high luminosities, caused by the presence of a large substructure outside the core. The effect of this substructure is diminished in the AGN model, where the extra feedback reduces the amount of cool, dense gas in the object.

The slope in the NR model does not evolve with redshift and remains ∼60 per cent of the present observed value. Some evolution is seen at low redshift for the radiative models, but when the core is excluded, there is no evidence for substantial evolution in any of the models. However, the change in normalization with redshift is much more interesting and can be seen in the bottom panels in Fig. 14. All radiative models predict higher luminosities at higher redshift (for a fixed mass) than expected from the self-similar model. Importantly, the amount of evolution is similar in the CSF, SFB and AGN models, but their normalization values are offset from one another at a given redshift. In general, the differences we see at $z = 0$ are largely replicated at the other redshifts. This suggests that the departure from self-similar evolution in the radiative models is largely driven by radiative cooling, with both feedback mechanisms largely serving to regulate the gas fraction, with AGN more effective in the inner region and supernovae further out. This is consistent with the entropy profile having a similar shape at $z = 0$ in all three radiative models.

6 RESOLUTION STUDY

An important issue that we have yet to discuss is the effect of numerical resolution. Resolution can be split into two components: the spatial resolution which is governed by the gravitational softening length (and minimum SPH smoothing length for the gas) and the mass resolution which is governed by the mass of the DM, gas and star particles.

In order to investigate mass resolution effects, new initial conditions were generated for our most massive cluster ($M_{200} \simeq 10^{15}\ h^{-1}M_{\odot}$) with 10 times fewer ($N_{200} \simeq 10^5$) and 10 times greater ($N_{200} \simeq 10^7$) particles than our default value ($N_{200} \simeq 10^6$). When the number of particles was increased, additional small-scale power was added in the initial conditions allowing smaller mass haloes to be resolved. We shall refer to this sequence of runs (going from the smallest to largest particle number) as VLR-LS, LR-MS and HR-SS, respectively. In all three cases, the softening lengths were computed using the method outlined in Power et al. (2003) and the minimum SPH smoothing length was set equal to this value. To specifically test the effect of spatial resolution, the LR and VLR clusters were also run with smaller softening lengths. Table 5 summarizes the details of the runs.

We first performed tests for the NR model, which allows us to check for the severity of two-body heating effects, expected to occur if the particle mass is too large and the softening too small. Such heating creates an artificial core in the density profile beyond the

Table 5. Details of the resolution tests performed. Column 1 lists the label given to each run; column 2 the approximate number of DM within r_{200}; column 3 the gas particle mass (in $10^8\ h^{-1}\,M_\odot$) and column 4 the maximum value of the (Plummer-equivalent) softening length (in h^{-1} kpc). Labels in bold represent runs with softening lengths chosen using the method outlined in Power et al. (2003).

Label	N_{200}	$m_{\rm gas}$	$\epsilon_{\rm max}$
VLR-LS	10^5	12.0	19.0
VLR-MS	10^5	12.0	6.0
VLR-SS	10^5	12.0	1.9
LR-MS	10^6	1.3	6.0
LR-SS	10^6	1.3	1.9
HR-SS	10^7	0.14	1.9

softening scale (i.e. for $r > 2.8\epsilon$), as energy is transferred from the DM to the gas. We found evidence for two-body heating in the VLR-MS, VLR-SS and LR-SS runs, somewhat vindicating our default choice of softening from Power et al. (2003). Two-body heating effects are reduced in the SFB case, as the cooling is able to dissipate this additional heat (Steinmetz & White 1997). This, however, does not mean that two-body heating is no longer an issue as it will still affect the evolution of the DM, which may in turn affect the gas and stars through changes to the gravitational potential. Given this complexity and the limited sample, one must be conservative about any conclusions drawn. For the remainder of this section, we focus on the AGN model only.

6.1 Black hole properties

Fig. 15 shows the growth of the central BH in the various runs (top panel), the $z = 0$ cumulative BH mass function for objects within r_{200} (middle) and the $z = 0$ central BH versus stellar bulge mass relation (bottom). It is immediately clear that the choice of softening length has a significant effect on the initial growth of the BH, while the mass resolution is less important. The VLR-SS, LR-SS and HR-SS runs, which all have softening lengths of $\epsilon = 1.9\ h^{-1}$ kpc, exhibit rapid, Eddington-limited growth until $a \simeq 0.2$. On the other hand, the VLR-MS and LR-MS runs (with $\epsilon = 6\,h^{-1}$ kpc) do not start growing rapidly until $a \simeq 0.3$. (We found that the BHs in the VLR-LS run were unable to grow at all, so do not show these here.) The softening length affects the accretion rate in two ways. First, the smaller softening results in a deeper gravitational potential around the BH, allowing a more rapid build-up of mass. Secondly, as the minimum SPH smoothing length is tied to the softening in our runs, a larger density is estimated for the gas local to the BH.

The smaller softening also allows the BHs associated with satellite galaxies to grow more efficiently, as can be seen from the BH mass function. Note that our default choice of resolution (LR-MS) produces the most massive BH, with the second most massive object being more than three orders of magnitude smaller. In addition to the effects of the softening on the accretion rate, we also checked whether the BH mass function is affected by overmerging of satellite BHs on to the central object; a smaller softening would make this less likely. However, we found this was not important, at least

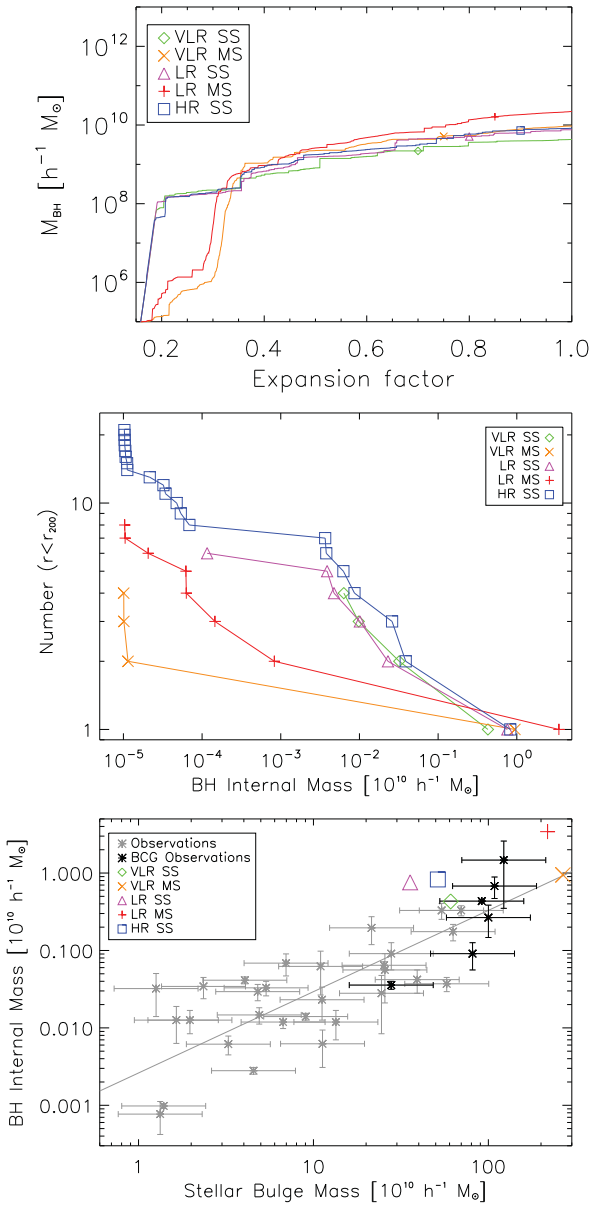

Figure 15. Growth of the largest BH with expansion factor (top panel), cumulative BH mass function within r_{200} at $z = 0$ (middle) and central BH mass versus bulge mass relation (bottom) for our most massive cluster, run with varying resolution and the AGN physics model.

for the most massive objects which are always associated with the same substructures.

Central BH mass versus stellar bulge mass is displayed in the bottom panel of Fig. 15. It is clear that, as well as affecting the growth of the largest BH, resolution also has an effect on the final mass of the stellar bulge. Runs with a smaller softening length produce a smaller bulge; efficient early growth (and therefore AGN feedback) is clearly important for the growth of the central BCG.

6.2 Star formation history

To further investigate the effect of resolution on the cluster's star formation history, we show in Fig. 16 the stellar mass formed by each value of a, which ends up within r_{200} at $a = 1$. We also split

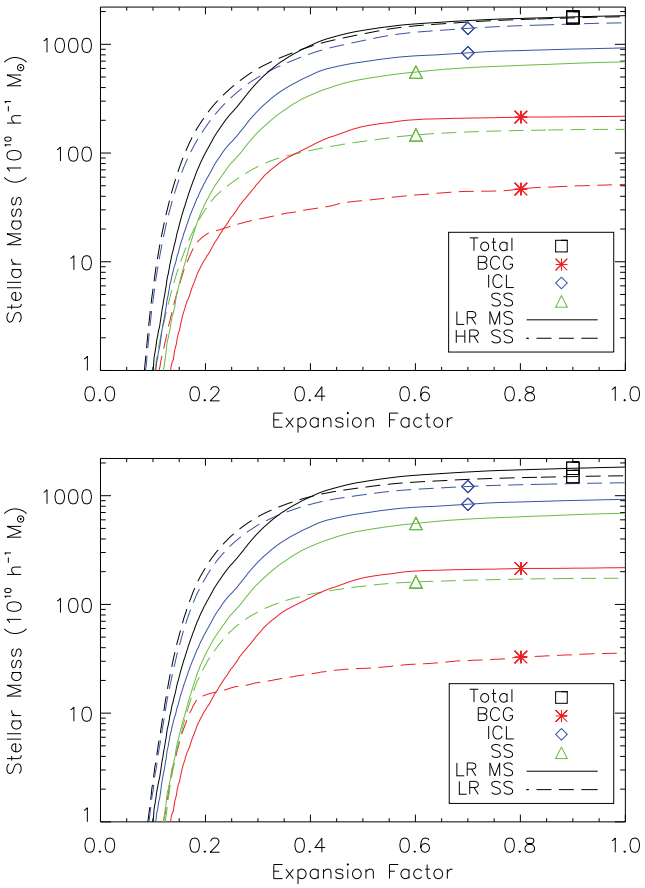

Figure 16. Cumulative stellar mass formed at each value of a, which ends up within r_{200} at $a = 1$. Solid curves are for the default LR-MS run, while the dashed curves are for the HR-SS (top panel) and LR-SS (bottom panel) runs. The results are also split into BCG, ICL and SS sub-components (as described in the legend).

this mass into the various sub-components (BCG, ICL and SS) as discussed in Section 3.2.

In the top panel, we compare our default-resolution (LR-MS; solid curves) to the higher-resolution simulation (HR-SS; dashed curves), while the effect of softening alone can be seen explicitly in the bottom panel (LR-MS with LR-SS; the VLR results are similar). Increasing the resolution makes little difference to the final stellar mass in the halo, although more stars form at early times ($a < 0.3$). This is expected, given that smaller mass objects can be resolved in the HR-SS simulation. However, some of the effect is also due to the change in softening length (as can be seen from comparing the solid and dashed curves in the bottom panel). As with the BHs, stars begin to form earlier when the softening length is smaller due to the deeper potential and higher gas densities in the halo centres.

As discussed above, the runs with smaller softening lengths also have significantly fewer stars in the BCG at $z = 0$, but this is also true for the other galaxies (SS). Consequently, the ICL mass has increased, so the runs with smaller softening lengths appear to have increased amounts of stripping. A simple explanation for this is that the stars in the sub-haloes are being puffed up due to two-body heating. While this would be expected to be larger in the LR-SS run (due to the smaller softening), it would also be less severe in HR-SS (due to the smaller DM particle mass). It is therefore unlikely that this is the cause, given that a similar increase in ICL mass is seen in both runs. An alternative explanation is that the stronger feedback at early times leads to cluster galaxies being less bound. Thus, more stars are stripped from the SS before they have a chance to merge with the central BCG.

This also has implications for the evolution of the BCG which, we find, grows much less rapidly at $z < 1$ in the runs with smaller softening lengths. In the LR-MS run, the BCG grows by almost a factor of 30 since $z = 1$ (cf. the sample median value of a factor of 5, as discussed in Section 3.2). However, in the LR-SS run (with the same mass resolution), the BCG has a slightly higher mass than the LR-MS object at $z = 1$ and grows by only a factor of 3 or so by $z = 0$. Again, nearly all the growth comes from dry mergers but the total mass in these merger events is now much smaller. Thus, in our model, the growth rate of BCGs at $z < 1$ is also sensitive to the adopted softening length but a slower rate (as desired) comes at the price of a larger ICL component. Simulations with higher resolution will be required to investigate this further, taking also the stellar mass function of galaxies into account.

6.3 Cluster profiles

The top-left panel of Fig. 17 displays the cumulative star fraction profile, allowing us to assess how resolution affects the final distribution of stars in the cluster. Again, much larger differences are seen when the softening length is varied: the SS runs have smaller star fractions in the core than the MS runs, due to the smaller BCG that has formed in the former cases. The effects of resolution on the cumulative gas fraction are more complex (top-right), exhibiting a dependence on both mass and spatial resolution. It is interesting to note that our standard set of runs [LR-MS and HR-SS, with a softening length that increases with particle mass according to the Power et al. (2003) formula] agree best outside the core. For the total baryon fraction profiles (not shown), a similar result to the star fraction profiles is seen in the core as the stars dominate the baryon budget in this region. However, on large scales ($r > 0.5\,r_{500}$) there is good convergence between all runs.

In the lower panels of Fig. 17, we show entropy and temperature profiles for the hot gas. We first consider the entropy profiles; as was the case with the hot gas fraction, the LR-MS and HR-SS runs show the best agreement outside the core. At fixed spatial resolution, decreasing the particle mass leads to a similar or larger entropy at fixed radius (e.g. going from VLR-SS → LR-SS → HR-SS). Similarly, increasing the softening length at fixed mass resolution also increases the entropy (e.g. LR-SS → LR-MS). These increases can largely be explained as due to decreases in gas density. Decreasing the softening length (at fixed mass resolution) produces more feedback at early times, as expected from the more efficient BH growth and star formation. This feedback is more effective in keeping the gas from forming stars in the cluster (hence also the lower star fractions in these runs), leading to a higher gas density (and thus lower entropy). However, decreasing the particle mass (at fixed softening length) has a smaller effect on the stellar and BH masses, suggesting that the effect on the hot gas is related to how well the outflows are resolved: higher mass resolution appears to lead to more effective outflows which move gas to larger radii. In summary, when going from LR-MS to HR-SS, the combined effects of less efficient star formation and more effective outflows approximately cancel, producing a similar entropy profile outside the core.

Inside the core, the entropy profiles show quite a lot of scatter, indicating that the core gas properties are sensitive to the choice of numerical parameters. The default LR-MS profile is much steeper than the others, a feature driven by the high gas density and low

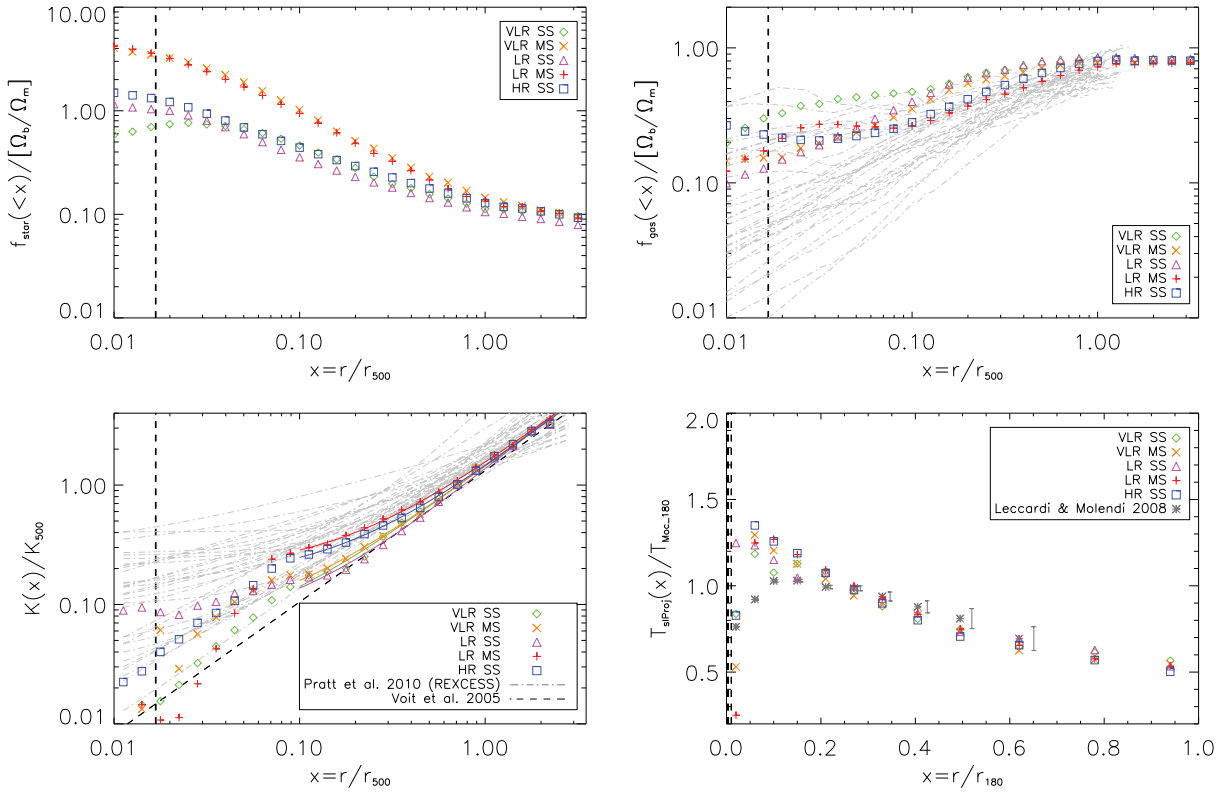

Figure 17. Radial gas and star profiles at $z = 0$ for the AGN runs with varying resolution. Clockwise from the top-left panel are the cumulative star fraction, hot gas fraction, projected spectroscopic-like temperature and entropy, respectively. The vertical dashed lines represent the minimum resolved scale for the SS and MS runs, respectively.

temperature within the central region. However, the highest resolution (HR-SS) run matches the observations the best across all radii, and the entropy within the core does not drop below those of CC clusters. Note that the distinctive feature at $\sim 0.06\, r_{500}$ is still present.

Finally, the spectroscopic-like temperature profiles are displayed in the bottom right of Fig. 17. Again, we have applied the method of Roncarelli et al. (2013), removing the densest gas within each bin. (We found that the removal of this gas is more important for runs with larger softening lengths, which show significantly more scatter from bin to bin.) In the radial range, $0.1 < r/r_{500} < 1$, all runs have similar temperature profiles; however, within the central region ($r < 0.05\, r_{500}$) the runs with larger softening lengths (VLR-MS and LR-MS) have very low temperatures. It can also be seen that the HR-SS run has the highest peak temperature and is therefore most discrepant with the observations. While this result is for one object, it suggests, as with our entropy profile, that we may be missing important physics in the cluster core.

7 SUMMARY AND DISCUSSION

There is now a wealth of observational data on clusters, offering an important opportunity to test how the different physics implemented in simulations affects the evolution of these massive objects. In this paper, results for a set of 30 clusters from the Millennium Gas simulation with a mass range of $10^{14}\, h^{-1}\, \mathrm{M}_\odot < M_{200} < 10^{15}\, h^{-1}\, \mathrm{M}_\odot$ were presented, with increasingly realistic sub-grid physics, in order to ascertain the effects of each physical process. The models implemented were a non-radiative (NR) model, which only included gravity and hydrodynamics; a model that also included radiative cooling and star formation (CSF); a model including supernova feedback (SFB), where powerful gas heating occurs (to 10^7 K) when a star is formed; and an AGN feedback model where a fixed fraction of energy from the accretion of mass on to a supermassive BH was used to heat the gas to high temperature (scaling with the virial temperature of the cluster). Each component is important in order to make progress towards the simulation of realistic clusters, which we summarize as follows.

(i) Radiative cooling permits gas to lose energy and become more dense as it flows to the centre of the cluster. The gas is then likely to undergo star formation, but without any form of feedback, too many stars are created, leading to the classic *overcooling* problem. However, cooling also causes higher entropy gas to flow inwards and this process is behind the similarity breaking seen in all our radiative models (as is evident from the entropy profile shapes and the redshift evolution of the X-ray luminosity–mass relation).

(ii) Supernova feedback provides energy to heat the gas surrounding stars and thus reduce the star formation rate. Although this energy is distributed throughout the cluster halo (in galaxies), it is only effective at larger radii: in the central region the energy released in supernovae is insufficient to prevent dense, cold gas cores that again result in forming too many stars.

(iii) Supermassive BHs are distributed throughout the cluster halo in galaxies; however, most of the energy released is from the largest black hole in the centre of the cluster. As a result, AGN feedback has a dramatic effect on the core gas, reducing the size of the central, BCG.

In order to ascertain the ideal properties for supernova and AGN feedback, different parameters were tested on both a low- and

high-mass halo, and compared to observations when appropriate. From this study, we conclude the following.

(i) While AGN feedback has an important effect on the star formation rate in the central region of the cluster, powerful supernova feedback is also required in order to reproduce the observed gas and star fractions within r_{500}.

(ii) The only AGN feedback parameter which has a large effect on the evolution of the cluster is the heating temperature. If a temperature is chosen that is too low, the heated gas is unable to escape the deep potential and instead creates a core of warm, dense gas. If the heating temperature is higher, gas then escapes out of the central region, reducing the gas density, but also taking most of the thermal energy with it.

(iii) A better match to the observed pressure profiles is obtained when the AGN heating temperature is tuned to scale with the final virial temperature of the halo. As such, the current model suffers from a fine-tuning problem.

(iv) While the AGN feedback efficiency has little effect on the cluster's evolution, it does allow the mass of the BH to be tuned; a lower efficiency allows the BH to become more massive and vice versa.

With the feedback parameters chosen as detailed above, our simulations with the AGN model are capable of reproducing a range of observable properties of clusters, including baryon, gas and star fraction within r_{500}; gas density and pressure profiles; and the Y_{SZ}–M_{500} and L_{bol}–M_{500} scaling relations. However, the simulations failed to resolve a number of issues. First, observables that are more sensitive to the temperature than the density of the gas are simulated with some success. A small number of low-entropy gas particles, both inside and outside substructures, serve to make the spectroscopic-like temperature much noisier than the mass-weighted temperature. When this gas was removed, the match to observations (especially outside the core) improves. A second issue is that while the AGN feedback significantly reduces the stellar mass fractions within BCGs, they are still around a factor of 3 larger than observed. A large part of this problem appears to be due to the fact that the AGN are not efficient enough at high redshift; a similar problem was seen by Ragone-Figueroa et al. (2013), who also performed cosmological simulations of clusters with (a different model of) AGN feedback. A third issue is that the entropy profiles in the AGN model do not match the observations inside the core region ($r < 0.15\,r_{500}$). A characteristic break is seen at this point, inside which the entropy declines rapidly to the centre. Further investigation revealed that the AGN heats and ejects gas from the central region, largely without disturbing the surrounding, cooling material. Creating the extreme profile of a non-cool-core cluster would require the core gas to be mixed much more efficiently than what is seen in our simulations, while cool-core clusters may be approximated with some additional variation in the heating temperature.

Finally, we considered the effect of varying the spatial and mass resolution for one of our clusters. We found that reducing the gravitational softening length (and thus also the minimum SPH smoothing length for the gas) had the largest effect on the BHs and stars; a smaller softening leads to earlier central BH growth and larger BHs in satellite galaxies. A smaller softening also affects the star formation history of the cluster, producing a smaller BCG, but more stars are found in the diffuse component. However, the resolution appears to affect the hot gas in a more complex way: outside the core, a higher spatial resolution and mass resolution increase and decrease the gas density, respectively, leading to broadly similar results. The highest resolution run produces a higher core entropy that is more consistent with cool-core clusters though the break in the profile remains. The problem with the X-ray temperatures also diminishes, but is still present, in the high-resolution runs.

7.1 Comparison with recent work

While this paper was being written, we became aware of two other new studies that are qualitatively similar to ours (i.e. designed to study the effects of AGN feedback on the galaxy cluster population). First, Planelles et al. (2014) performed simulations of 29 Lagrangian regions, producing 160 objects down to group scales (see also Planelles et al. 2013). We subsequently refer to this work as P14. Secondly, Le Brun et al. (2014) analysed a set of large-volume (400 h^{-1} Mpc) cosmological simulations with AGN feedback (cosmo-OWLS). Their analysis also goes down to group scales and state that there are approximately 14 000 objects in their non-radiative run at $z = 0$. We refer to this work as LeB14.

All three studies differ in the cosmological model adopted, the resolution of the simulations and the implementation of the sub-grid physics. Regarding cosmological parameters, LeB14 adopt values derived from *Planck* data for their main results; the main relevant change is the baryon fraction, which decreases from ∼0.17 for our study (and that of P14) to ∼0.15. A lower baryon fraction will reduce the efficiency of radiative cooling (for a fixed metallicity and temperature) and therefore not require as much feedback to reproduce the observed ratio of gas to stars.

For numerical resolution, our default DM particle mass varies such that the approximate number of particles within r_{200}, $N_{200} \simeq 10^6$. In P14 and LeB14, the particle mass is kept constant so N_{200} varies with halo mass. For the same range of masses as our sample ($M_{200} = 1$–$10 \times 10^{14}\ h^{-1}\,M_\odot$), $N_{200} \simeq 10^5$–10^6 for P14 (thus matching our resolution for the most massive objects) and $N_{200} \simeq 2 \times (10^4$–$10^5)$ for LeB14 (i.e. at least a factor of 5 smaller than ours). Regarding the gravitational softening length, P14 and LeB14 use similar values to ours (5 and 4 h^{-1} kpc respectively); however, both studies allow the SPH smoothing length to decrease below this value (by a factor of 2 and 5, respectively). As we discussed in Section 6, a smaller softening length (and SPH smoothing length) has a significant impact on the growth of the BHs and star formation rate. While this may be necessary in order to grow BHs when the resolution is low, one also has to be cautious given that a smaller value can also lead to spurious two-body heating effects.

For the gas physics, both P14 and LeB14 include metal-dependent cooling whereas our study assumed a metal-free gas. Including metals would likely require us to re-tune the feedback parameters due to the increase in cooling efficiency; this will be especially true at high redshift, where the gas density is higher and temperatures lower. As in our case, P14 and LeB14 also include supernovae-driven winds in their main simulations, but add the energy in kinetic form whereas we adopt the thermal feedback approach. Such models ought to produce a similar outcome when the cooling time of the gas is sufficiently long, but the limited resolution of the simulations will likely lead to some differences. Finally, regarding the AGN feedback, our study and LeB14 both used the method of Booth & Schaye (2009), whereby energy is stored until there is enough to heat one particle to a fixed temperature, T_{AGN}, whereas P14 use the kernel-weighted feedback implementation of Springel et al. (2005a), where the energy is shared immediately between nearby gas particles. A key difference between the AGN model in this paper and those in LeB14 is that we use a value of T_{AGN} that scales with the final virial temperature of the halo, whereas they find $T_{AGN} = 10^8$ K gives the best results over their whole mass range.

As with the work presented in this paper, both P14 and LeB14 find that their AGN feedback models are in good agreement with observational data for many global properties (e.g. gas and star fractions, X-ray and SZ scaling relations). One property that our models do not predict as well as the others is the X-ray temperature of the cluster gas; in our case, we must remove the densest gas otherwise it substantially down-weights the spectroscopic-like temperature. The reason for this is unclear; however, we first note that LeB14 estimate temperatures by directly fitting plasma models to simulated X-ray spectra, as is done for the observations (they also adopt hydrostatic mass estimates in the scaling relations and thus factor in the effect of hydrostatic mass bias, which we ignore in this paper due to the problems encountered with temperature measurements). It may be that the spectroscopic-like formula is incorrectly tuned to the radiative simulations presented here (Mazzotta et al. 2004 used non-radiative simulations in their study). However, P14 also use $T_{\rm sl}$ in their analysis, suggesting that the cold, dense gas in their simulations (which are of similar resolution to ours for high-mass objects) is less of a problem. It may be that metal enrichment plays a part (allowing more rapid cooling out of the hot phase). Alternatively, the smaller adopted minimum SPH smoothing length could affect the results, allowing gas to reach higher density and cool more efficiently. As discussed in Section 6, this can have a noticeable effect on the core temperatures.

Gas density and entropy profiles in LeB14 match those in our own work over the radial ranges displayed, which is unsurprising considering the similarity of the feedback models. However, our simulations have higher resolution, allowing us to probe smaller radii where the entropy and temperature are too low, whilst the gas density is too high. It should also be noted that LeB14 achieved their best match to observations using a fixed AGN heating temperature. However, as they allude to in their conclusions, the lower baryon fraction in the *Planck* cosmology appears to play an important role in this difference (I. McCarthy, private communication). Finally, we note that the pressure profile of P14 matches the observations (and therefore, by design, our own results). However, although our entropy profiles agree with theirs outside the core, there are noticeable differences within this region (P14 overestimate the observed core entropy). Interestingly, unlike the simulations presented in this paper (or those in LeB14), the gas profiles presented in P14 seem very similar in their runs with and without AGN feedback on cluster scales, with only the stellar fractions in being affected by the AGN. It thus seems that their implementation of AGN feedback, whilst key in regulating the star formation, does not significantly affect gas profiles.

In conclusion, our study reinforces those of P14 and LeB14 that simulations incorporating radiative cooling and simple models for the feedback of energy from supernovae and AGN are able to successfully reproduce many key observational properties of clusters. However, a detailed match to the spatial distribution of gas and stars is still wanting, especially in the cluster cores. An important step forward will be to compare many of the AGN models run on the same initial conditions, so we can remove the uncertainty from cosmological parameters and numerical resolution. This, combined with progress in modelling cluster physics and performing higher resolution simulations (an important but reachable goal will be to resolve the Jeans length of warm interstellar gas), should allow us to produce even more realistic cluster simulations and understand more about their formation and evolutionary history. Such progress will be crucial for improving the use of clusters as cosmological probes and our understanding of galaxy formation in extreme environments.

ACKNOWLEDGEMENTS

The simulations used in this paper were performed on the ICC Cosmology Machine, which is part of the DiRAC Facility jointly funded by STFC, Large Facilities Capital Fund of BIS and Durham University. SRP and RDAN were both supported by STFC studentships while this work was being done. RDAN also acknowledges the support received from the Jim Buckee Fellowship. STK, PAT and ARJ acknowledge support from STFC, grant numbers ST/L000768/1, ST/J000652/1 and ST/I001166/1, respectively.

REFERENCES

Andersson K. et al., 2011, ApJ, 738, 48
Arnaud M., Pointecouteau E., Pratt G. W., 2005, A&A, 441, 893
Arnaud M., Pointecouteau E., Pratt G. W., 2007, A&A, 474, L37
Arnaud M., Pratt G. W., Piffaretti R., Böhringer H., Croston J. H., Pointecouteau E., 2010, A&A, 517, A92
Babul A., Balogh M. L., Lewis G. F., Poole G. B., 2002, MNRAS, 330, 329
Balogh M. L., Pearce F. R., Bower R. G., Kay S. T., 2001, MNRAS, 326, 1228
Battaglia N., Bond J. R., Pfrommer C., Sievers J. L., 2012, ApJ, 758, 74
Böhringer H. et al., 2007, A&A, 469, 363
Booth C. M., Schaye J., 2009, MNRAS, 398, 53
Booth C. M., Schaye J., 2010, MNRAS, 405, L1
Borgani S., Governato F., Wadsley J., Menci N., Tozzi P., Lake G., Quinn T., Stadel J., 2001, ApJ, 559, L71
Borgani S., Governato F., Wadsley J., Menci N., Tozzi P., Quinn T., Stadel J., Lake G., 2002, MNRAS, 336, 409
Borgani S. et al., 2004, MNRAS, 348, 1078
Bryan G. L., 2000, ApJ, 544, L1
Budzynski J. M., Koposov S. E., McCarthy I. G., Belokurov V., 2014, MNRAS, 437, 1362
Burke C., Collins C. A., Stott J. P., Hilton M., 2012, MNRAS, 425, 2058
Crain R. A., Eke V. R., Frenk C. S., Jenkins A., McCarthy I. G., Navarro J. F., Pearce F. R., 2007, MNRAS, 377, 41
Croston J. H. et al., 2008, A&A, 487, 431
da Silva A. C., Kay S. T., Liddle A. R., Thomas P. A., 2004, MNRAS, 348, 1401
Dalla Vecchia C., Schaye J., 2012, MNRAS, 426, 140
Davé R., Katz N., Weinberg D. H., 2002, ApJ, 579, 23
Davis M., Efstathiou G., Frenk C. S., White S. D. M., 1985, ApJ, 292, 371
Dubois Y., Devriendt J., Teyssier R., Slyz A., 2011, MNRAS, 417, 1853
Eckert D., Molendi S., Vazza F., Ettori S., Paltani S., 2013, A&A, 551, A22
Evrard A. E., Henry J. P., 1991, ApJ, 383, 95
Fabian A. C., 2012, ARA&A, 50, 455
Fabjan D., Borgani S., Tornatore L., Saro A., Murante G., Dolag K., 2010, MNRAS, 401, 1670
Gaspari M., Melioli C., Brighenti F., D'Ercole A., 2011, MNRAS, 411, 349
Giodini S. et al., 2009, ApJ, 703, 982
Gonzalez A. H., Zabludoff A. I., Zaritsky D., 2005, ApJ, 618, 195
Gonzalez A. H., Zaritsky D., Zabludoff A. I., 2007, ApJ, 666, 147
Guo Q., White S., Angulo R. E., Henriques B., Lemson G., Boylan-Kolchin M., Thomas P., Short C., 2013, MNRAS, 428, 1351
Hardcastle M. J., Krause M. G. H., 2013, MNRAS, 430, 174
Hoyle F., Lyttleton R. A., 1939, Proc. Camb. Phil. Soc., 35, 405
Jenkins A., 2013, MNRAS, 434, 2094
Kaiser N., 1991, ApJ, 383, 104
Kay S. T., 2004, MNRAS, 347, L13
Kay S. T., Thomas P. A., Theuns T., 2003, MNRAS, 343, 608
Kay S. T., Peel M. W., Short C. J., Thomas P. A., Young O. E., Battye R. A., Liddle A. R., Pearce F. R., 2012, MNRAS, 422, 1999
Komatsu E. et al., 2011, ApJS, 192, 18
Le Brun A. M. C., McCarthy I. G., Schaye J., Ponman T. J., 2014, MNRAS, 441, 1270 (LeB14)
Leccardi A., Molendi S., 2008, A&A, 486, 359
Lidman C. et al., 2012, MNRAS, 427, 550

Marrone D. P. et al., 2012, ApJ, 754, 119
Mazzotta P., Rasia E., Moscardini L., Tormen G., 2004, MNRAS, 354, 10
McCarthy I. G. et al., 2010, MNRAS, 406, 822
McCarthy I. G., Schaye J., Bower R. G., Ponman T. J., Booth C. M., Dalla Vecchia C., Springel V., 2011, MNRAS, 412, 1965
McConnell N. J., Ma C.-P., 2013, ApJ, 764, 184
McNamara B. R., Nulsen P. E. J., 2012, New J. Phys., 14, 055023
Morsony B. J., Heinz S., Brüggen M., Ruszkowski M., 2010, MNRAS, 407, 1277
Muanwong O., Thomas P. A., Kay S. T., Pearce F. R., Couchman H. M. P., 2001, ApJ, 552, L27
Muanwong O., Thomas P. A., Kay S. T., Pearce F. R., 2002, MNRAS, 336, 527
Nagai D., 2006, ApJ, 650, 538
Nagai D., Vikhlinin A., Kravtsov A. V., 2007a, ApJ, 655, 98
Nagai D., Kravtsov A. V., Vikhlinin A., 2007b, ApJ, 668, 1
Newton R. D. A., Kay S. T., 2013, MNRAS, 434, 3606
Pearce F. R., Thomas P. A., Couchman H. M. P., Edge A. C., 2000, MNRAS, 317, 1029
Planck Collaboration, 2011, A&A, 536, A11
Planck Collaboration, 2013, A&A, 550, A131
Planelles S., Borgani S., Dolag K., Ettori S., Fabjan D., Murante G., Tornatore L., 2013, MNRAS, 431, 1487
Planelles S., Borgani S., Fabjan D., Killedar M., Murante G., Granato G. L., Ragone-Figueroa C., Dolag K., 2014, MNRAS, 438, 195 (P14)
Ponman T. J., Cannon D. B., Navarro J. F., 1999, Nature, 397, 135
Ponman T. J., Sanderson A. J. R., Finoguenov A., 2003, MNRAS, 343, 331
Power C., Navarro J. F., Jenkins A., Frenk C. S., White S. D. M., Springel V., Stadel J., Quinn T., 2003, MNRAS, 338, 14
Power C., Nayakshin S., King A., 2011, MNRAS, 412, 269
Power C., Read J. I., Hobbs A., 2014, MNRAS, 440, 3243
Pratt G. W., Croston J. H., Arnaud M., Böhringer H., 2009, A&A, 498, 361
Pratt G. W. et al., 2010, A&A, 511, A85
Puchwein E., Sijacki D., Springel V., 2008, ApJ, 687, L53
Puchwein E., Springel V., Sijacki D., Dolag K., 2010, MNRAS, 406, 936
Ragone-Figueroa C., Granato G. L., Murante G., Borgani S., Cui W., 2013, MNRAS, 436, 1750
Roncarelli M., Ettori S., Borgani S., Dolag K., Fabjan D., Moscardini L., 2013, MNRAS, 432, 3030
Schaye J., Dalla Vecchia C., 2008, MNRAS, 383, 1210
Shaver P. A., Wall J. V., Kellermann K. I., Jackson C. A., Hawkins M. R. S., 1996, Nature, 384, 439
Short C. J., Thomas P. A., Young O. E., Pearce F. R., Jenkins A., Muanwong O., 2010, MNRAS, 408, 2213
Short C. J., Thomas P. A., Young O. E., 2013, MNRAS, 428, 1225
Sifón C. et al., 2013, ApJ, 772, 25
Sijacki D., Springel V., Di Matteo T., Hernquist L., 2007, MNRAS, 380, 877
Springel V., 2005, MNRAS, 364, 1105
Springel V., White S. D. M., Tormen G., Kauffmann G., 2001, MNRAS, 328, 726
Springel V., Di Matteo T., Hernquist L., 2005a, MNRAS, 361, 776
Springel V. et al., 2005b, Nature, 435, 629
Springel V. et al., 2008, MNRAS, 391, 1685
Steinmetz M., White S. D. M., 1997, MNRAS, 288, 545
Stott J. P., Collins C. A., Burke C., Hamilton-Morris V., Smith G. P., 2011, MNRAS, 414, 445
Stott J. P. et al., 2012, MNRAS, 422, 2213
Sun M., 2012, New J. Phys., 14, 045004
Sunyaev R. A., Zeldovich Y. B., 1972, Comments Astrophys. Space Phys., 4, 173
Sutherland R. S., Dopita M. A., 1993, ApJS, 88, 253
Thomas P. A., Couchman H. M. P., 1992, MNRAS, 257, 11
Tornatore L., Borgani S., Springel V., Matteucci F., Menci N., Murante G., 2003, MNRAS, 342, 1025
Vikhlinin A., Kravtsov A., Forman W., Jones C., Markevitch M., Murray S. S., Van Speybroeck L., 2006, ApJ, 640, 691
Voit G. M., Bryan G. L., 2001, Nature, 414, 425
Voit G. M., Kay S. T., Bryan G. L., 2005, MNRAS, 364, 909
Voit G. M., Cavagnolo K. W., Donahue M., Rafferty D. A., McNamara B. R., Nulsen P. E. J., 2008, ApJ, 681, L5
Wu K. K. S., Fabian A. C., Nulsen P. E. J., 2000, MNRAS, 318, 889

APPENDIX A: MEASURING SIMULATED CLUSTER PROPERTIES

In this appendix, we summarize how various cluster properties are estimated from the simulated data. For each cluster, we start with a list of all gas, star and DM particles that are located within a radial distance $r < r_\Delta$ from the position of the most bound particle (as found by SUBFIND). The outer radius, r_Δ, is defined in the usual way,

$$M_\Delta = \frac{4}{3}\pi\,\Delta\,\rho_{\rm cr}(z)\,r_\Delta^3, \tag{A1}$$

where M_Δ is the total enclosed mass and $\rho_{\rm cr}(z)$ is the critical density. By default, we set $\Delta = 500$ but occasionally use other values where appropriate. Hot gas is defined as those gas particles with temperatures $T > 10^6$ K except when X-ray temperatures are estimated (see below). When estimating cluster profiles, we sub-divide the cluster volume into spherical shells, equally spaced in $\log_{10}(r/r_{500})$.

Baryon, hot gas and star fractions are calculated via

$$f_{\rm type} = \frac{\sum_{i=1}^{N_{\rm type}} m_i}{\sum_{i=1}^{N} m_i}, \tag{A2}$$

where *type* refers to gas, stars or both (with total number $N_{\rm type}$); m_i is the mass of the ith particle and N is the total number of particles (including DM) in the region being summed. The mass density of each species is similarly calculated as

$$\rho_{\rm type} = \frac{1}{V}\sum_{i=1}^{N_{\rm type}} m_i, \tag{A3}$$

where the V is the volume of the region where the density is being estimated. For example, the density profile is estimated using concentric spherical shells, each with volume $V = (4\pi/3)(r_{\rm out}^3 - r_{\rm in}^3)$, where $r_{\rm in}$ and $r_{\rm out}$ are the inner and outer shell radii, respectively.

For the electron pressure of the hot gas ($P_{\rm e} = n_{\rm e}kT$), we use

$$P_{\rm e} = \frac{1}{V}\frac{k}{\mu_{\rm e} m_{\rm H}}\sum_{i=1}^{N_{\rm hot}} m_i T_i, \tag{A4}$$

where T_i is the temperature of the ith hot gas particle and $\mu_{\rm e} = 1.14$ is the assumed mean atomic weight per free electron. Similarly, we estimate the entropy ($K \equiv kT/n_{\rm e}^{2/3}$) using

$$K = V^{2/3}k(\mu_{\rm e} m_{\rm H})^{2/3}\,\frac{\sum_{i=1}^{N_{\rm hot}} m_i T_i}{\left(\sum_{i=1}^{N_{\rm hot}} m_i\right)^{5/3}}. \tag{A5}$$

When presenting pressure and entropy profiles, we follow convention and express these quantities in units of a characteristic scale, appropriate for self-similar, isothermal systems (e.g. Nagai, Kravtsov & Vikhlinin 2007b). Starting from a characteristic density

$$\rho_{500} = 500\,(\Omega_{\rm b}/\Omega_{\rm m})\,\rho_{\rm cr}(z) = \left[\frac{1500}{8\pi G}\right]\,(\Omega_{\rm b}/\Omega_{\rm m})\,H(z)^2 \tag{A6}$$

and temperature

$$kT_{500} = \frac{GM_{500}\mu m_{\rm H}}{2r_{500}} = 5\mu m_{\rm H}\left[\frac{GH(z)M_{500}}{2}\right]^{2/3}, \tag{A7}$$

the entropy scale can be written as

$$K_{500} = \left[\frac{4\pi^2 G^4 \mu^3 \mu_e^2 m_H^5}{4500(\Omega_b/\Omega_m)^2}\right]^{1/3} H(z)^{-2/3} M_{500}^{2/3}, \quad \text{(A8)}$$

where $\rho_{cr} = 3H^2/(8\pi G), H(z) = H_0 E(z) = H_0[\Omega_m(1+z)^3 + \Omega_\Lambda]^{1/2}$ is the Hubble parameter (assuming a flat universe) and $\mu = 0.59$ is the mean atomic weight for a fully ionized, primordial gas. Similarly, for the pressure scale

$$P_{500} = \frac{3(\Omega_b/\Omega_m)(\mu/\mu_e)}{8\pi}\left[\frac{500}{2G^{1/4}}\right]^{4/3} H(z)^{8/3} M_{500}^{2/3}. \quad \text{(A9)}$$

When X-ray temperatures are presented, we use the approximation suggested by Mazzotta et al. (2004)

$$T_{sl} = \frac{\sum_{i=1}^{N_X} \rho_i T_i^{1/4}}{\sum_{i=1}^{N_X} \rho_i T_i^{-3/4}}, \quad \text{(A10)}$$

where N_X is the number of particles with $kT > 0.5$ keV. For hot clusters ($kT > 2$ keV), this spectroscopic-like temperature was shown to be a better estimate of the X-ray temperature than a simple mass-weighted temperature and preferentially weights cooler, denser gas. [Note, however, that we have not checked if the weighting is optimal for the models presented in this paper; Mazzotta et al. (2004) tuned it to non-radiative simulations.] As discussed in Section 2, we found that this estimate is significantly affected by the presence of a small number of dense gas particles that may be spurious due to the lack of entropy mixing in standard SPH. To reduce this effect, we adopt the method discussed in Roncarelli et al. (2013), which starts by ranking all gas particles in each radial shell (used to calculate profiles) by volume, $V_i = m_i/\rho_i$. Particles with the largest V_i that make up 99 per cent of the shell volume are retained and the rest (which are the densest particles by construction) discarded.

Finally, we also consider two integrated properties, both observable: the bolometric X-ray luminosity and the SZ Y parameter. The luminosity is estimated as

$$L_{bol} = \frac{m_{gas}}{(\mu m_H)^2} \sum_{i=1}^{N_{hot}} \rho_i \, \Lambda(T_i, Z), \quad \text{(A11)}$$

where ρ_i is the SPH density of the ith hot gas particle and $\Lambda(T, Z)$ is the same cooling function used in the simulation. Although we assume $Z = 0$ for our main radiative runs, we adopt $Z = 0.3\,Z_\odot$ when calculating luminosities as this is the typical metallicity of the ICM.

Cluster cores are the hardest part to simulate and both L_{bol} and T_{sl} are dominated by the central region. Results excluding gas from the inner region ($r < 0.15 r_{500}$) will therefore also be considered for these quantities and written as $L_{bol,\,OC}$ and $T_{sl,\,OC}$ for the luminosity and temperature, respectively.

For the SZ Y parameter, we absorb the angular diameter dependence

$$D_A^2 Y_{SZ} = \frac{\sigma_T m_{gas} k}{\mu_e m_H m_e c^2} \sum_{i=1}^{N_{hot}} T_i. \quad \text{(A12)}$$

This quantity is proportional to the total thermal energy of the hot gas and ought to be less sensitive to cooling and feedback processes than the X-ray luminosity.

APPENDIX B: OBSERVATIONAL DATA

We use a number of results from observational data sets to compare with our simulations in this paper. First, we compare our baryon, hot gas and star fractions with the observational constraints from Giodini et al. (2009). They analysed 91 groups and poor clusters at redshift, $0.1 < z < 1$, selected from the COSMOS 2 deg^2 survey, and 27 nearby clusters with robust total and stellar masses inside r_{500}. For hot gas fractions, we also make use of the *XMM–Newton* results of Arnaud et al. (2007) for a sample of 10 relaxed clusters, and the larger REXCESS sample (Böhringer et al. 2007), with data taken from Croston et al. (2008). The REXCESS sample is a representative sample of low-redshift X-ray clusters and contains 33 objects over a mass range $10^{14} < M_{500}/M_\odot < 10^{15}$. We also use this sample when comparing our gas density (Croston et al. 2008) and entropy (Pratt et al. 2010) profiles, as well as our X-ray scaling relations between luminosity, temperature and mass (Pratt et al. 2009).

For the star fractions, we additionally compare our results with the best-fitting relation (between star fraction and halo mass) presented in Budzynski et al. (2014). In that study, 20 171 large groups and clusters with a mass $M_{500} > 10^{13.7}\,M_\odot$ were optically selected from Sloan Digital Sky Survey (SDSS) data at $0.15 < z < 0.4$. The objects were then separated into four mass bins and stacked in order to calculate more robust stellar fractions (including the contribution from a low surface brightness component).

When presenting temperature profiles, we compare our results with those from Leccardi & Molendi (2008), where 50 objects were selected with $M_{500} > 10^{14}\,M_\odot$ and observed with *XMM–Newton*. Some of these objects are also in the REXCESS sample. For the pressure profiles, we compare against fits to the total, cool-core and non-cool-core samples by Planck Collaboration (2013). They analysed *Planck* SZ + *XMM–Newton* X-ray data for 62 nearby massive clusters with a mass range of $2 \times 10^{14} < M_{500}/M_\odot < 2 \times 10^{15}$. We also compare our simulated Y_{SZ}–M_{500} relations against the results from an earlier study by the Planck Collaboration using the same data (Planck Collaboration 2011).

This paper has been typeset from a TEX/LATEX file prepared by the author.